Using Novel Lake-Based Snowfall Measurements from Sites in the Alps, Himalayas, and Rockies to Evaluate Snowfall Estimates from Atmospheric Simulations Using the High-Resolution Regional Met Office Unified Model

SIDDHARTH GUMBER,[a] ANDREW ORR,[a] PAUL FIELD,[b,c] FEDERICO COVI,[a] HAMISH D. PRITCHARD,[a] PRANAB DEB,[d] MARC GIRONA-MATA,[a,e] TONY PHILLIPS,[a] EMILY POTTER,[f] CHANDNI THAKUR,[g] AND MARTIN WIDMANN[g]

[a] *British Antarctic Survey, United Kingdom Research and Innovation, Cambridge, United Kingdom*
[b] *Met Office, Exeter, United Kingdom*
[c] *School of Earth and Environment, University of Leeds, Leeds, United Kingdom*
[d] *Centre for Oceans, Rivers, Atmosphere and Land Sciences, Indian Institute of Technology, Kharagpur, India*
[e] *Department of Engineering, University of Cambridge, Cambridge, United Kingdom*
[f] *School of Geography and Planning, University of Sheffield, Sheffield, United Kingdom*
[g] *School of Geography, Earth and Environmental Sciences, University of Birmingham, Birmingham, United Kingdom*

(Manuscript received 20 August 2025, in final form 15 June 2026, accepted 7 July 2026)

ABSTRACT: The complex terrain in mountainous regions makes it extremely difficult to accurately measure or model snowfall, which is a key component of the terrestrial water budget. This study addresses these challenges by using high-altitude frozen lakes as pressure-sensing surfaces to produce accurate observations of the water content of snowfall at a range of sites in the European Alps, west–central Himalayas, and central Rockies, which are subsequently used to test and constrain snowfall output from a 1.5-km resolution version of the atmosphere-only Met Office Unified Model (MetUM). The model resolution is on a similar scale to the size of the lakes, as well as sufficiently fine to represent the critical interactions between atmospheric flows and the complex orography that influences snowfall and especially extremes. The snowfall output from the MetUM is additionally fine tuned by adjusting the fall speed of snow particles so that it is best able to capture the observed snowfall amounts, especially for extreme events. The results presented here show that the MetUM is generally able to accurately simulate both the timing and amounts of the snowfall observations over mountainous regions. Moreover, the model is particularly good at representing extreme snowfall events, with our study also using model hydrometeor output to examine the microphysical conditions related to these conditions. Finally, we suggest that the model output can effectively be used as pseudo-observations and for the generation of high-resolution, long-term gridded snowfall products.

SIGNIFICANCE STATEMENT: Snowfall in mountainous regions is a vital source of freshwater, sustaining rivers that support both large populations and diverse ecosystems. However, the complex topography of these areas poses significant challenges for accurately measuring snowfall. This study tackles these difficulties by using high-altitude frozen lakes as natural pressure sensors to monitor snowfall water content across sites in the European Alps, the west–central Himalayas, and the central Rockies. These observations are used to constrain and refine snowfall simulations from a high-resolution version of the Met Office Unified Model. The results show that the model can accurately simulate both the timing and amounts of the snowfall observations and can effectively be used for the generation of long-term snowfall products.

KEYWORDS: Snowfall; Numerical weather prediction/forecasting; Model evaluation/performance; Regional models; Field experiments; Mountain meteorology

1. Introduction

Snowfall occurring in mountainous regions during winter provides a crucial source of freshwater for rivers during spring and summer when it is released by melting, providing an essential resource for large populations and terrestrial ecosystems (Barnett et al. 2005; Pritchard et al. 2021; Wester et al. 2019; Immerzeel et al. 2020). Snowfall is also the principal source of mass for all the world's mountain glaciers, another critical natural reservoir (Pritchard 2019). However, despite its importance, the amount of falling and accumulated snow in such orographically complex regions remains one of the least observed, least understood, and most uncertain components of the terrestrial water budget (Pritchard 2021; Immerzeel et al. 2020). For example,

Denotes content that is immediately available upon publication as open access.

Supplemental information related to this paper is available at the Journals Online website: https://doi.org/10.1175/MWR-D-25-0194.s1.

Corresponding author: Siddharth Gumber, sidmba@bas.ac.uk, siddharthbts@outlook.com

DOI: 10.1175/MWR-D-25-0194.1

uncertainties in the amount of snow and its spatiotemporal distribution in mountainous regions lead to errors in hydrological models, resulting in flawed predictions of streamflow (Karki et al. 2017; Shannon et al. 2023; Tobin et al. 2012). This knowledge gap also limits our ability to predict the impacts of climate change on the amount and seasonality of streamflow, with snow amounts projected to decline in many mountainous regions throughout the twenty-first century due to warming (Immerzeel et al. 2010; Pörtner et al. 2022; Hock et al. 2019; Pritchard 2019; Viviroli et al. 2011), with far-reaching implications for water resources, food security, energy systems, and livelihoods (Wester et al. 2019; Wijngaard et al. 2017; Orr et al. 2022; Ghosh et al. 2023). Furthermore, it hinders our understanding of the occurrence of hydrometeorological hazards including avalanches triggered by extreme snowfall events and flooding caused by the rapid melting of snow by warm extremes (Sun et al. 2024; Ortner et al. 2023), and hence, improving our understanding of snowfall in mountainous regions is an urgent scientific priority (Orr et al. 2022; Sabin et al. 2020).

Quantifying mountain snowfall is highly challenging for a number of reasons. For example, the typical remote location of mountains complicates the installation and maintenance of instruments to measure snowfall, resulting in sparse observational networks, especially at high altitudes (Ohara et al. 2011; Derin et al. 2016; Milly and Dunne 2002; Rasmussen et al. 2012). This is especially problematic for High Mountain Asia (HMA), with the Global Historical Climatology Network (GHCN) database of station data (Menne et al. 2012) including only one long-running precipitation-monitoring station to represent 500 000 km^2 of Asia's Himalayan headwaters above 4000-m altitude, leading to significant snowfall-related uncertainties for this region (Pritchard 2021). Such sparse networks of instruments are unable to represent the considerable small-scale spatiotemporal variability of snowfall (including extremes) that occurs in mountainous regions such as HMA, which are heavily influenced by a wide variety of local micrometeorological conditions that are tied to their complex orography (Orr et al. 2017; Archer and Fowler 2004; Bannister et al. 2019; Immerzeel et al. 2015; Bookhagen and Burbank 2010; Baudouin et al. 2020; Pritchard 2021; Roe 2005; Houze 2012). Finally, although various field-based techniques have been developed to measure snowfall, all have significant limitations that contribute to sizeable biases in estimating the snow water equivalent (SWE) (Pritchard et al. 2021). In particular, the widely used heated pluviometers (also known as rain gauges) are prone to considerable wind-induced undercatch errors of snowfall, which can reach up to 78% in strong wind conditions (Goodison et al. 1998), and all observe a very small (meter scale) area of the landscape.

Such gauge data have been widely used to develop gridded precipitation datasets, including daily products like the Asian Precipitation–Highly Resolved Observational Data Integration Towards Evaluation of Water Resources (APHRODITE; Yatagai et al. 2012) dataset, which includes HMA, and the Alpine Precipitation Grid Dataset (APGD; Isotta et al. 2014), which includes the European Alps. However, the application of these products in mountainous regions remains questionable due to the above concerns over the sparseness and quality of the snowfall data, as well as inadequacies in interpolation methods (Mishra et al. 2023). For example, these products typically systematically underestimate snowfall at high altitudes, in contrast to better agreement with snowfall observations in relatively low-altitude areas where data are more widely available and of better quality (Currier et al. 2017; Gutmann et al. 2012; Hiemstra et al. 2006). Tested against streamflow measurements, monthly gridded global precipitation datasets including WorldClim, version 2 (based on GHCN gauge data), for example, were found to systematically underestimate precipitation in the mountain cryosphere by 50%–100% (Beck et al. 2020), i.e., consistent with considerable wind-induced undercatch errors associated with pluviometers. Even in the relatively extensively monitored European Alps, WorldClim v2 requires bias correction factors ranging from 1 to 1.5 (Pritchard 2021; Beck et al. 2020). Furthermore, satellite-based, gridded, precipitation datasets such as the Tropical Rainfall Measuring Mission (TRMM; Huffman et al. 2007) also struggle to represent snowfall over mountainous regions, particularly over glaciated areas (Yang et al. 2024; Andermann et al. 2011; Yin et al. 2008). However, there has also been some success in using remote sensing constrained snow reconstructions and streamflow observations to back calculate the spatiotemporal distribution of precipitation in mountainous locations (Pflug et al. 2022; Henn et al. 2018). Consequently, snowfall estimates from the various gridded datasets available can differ substantially in both their climatological and extreme values, underscoring our limited understanding of snowfall amounts and its spatiotemporal distribution in mountainous regions (Bannister et al. 2019; Palazzi et al. 2013).

Snowfall estimates from global reanalysis products like the fifth generation European Centre for Medium-Range Weather Forecasts (ECMWF) atmospheric reanalysis (ERA5; Hersbach et al. 2020) have also been used to analyze variability and trends in mountainous regions, including the European Alps (Monteiro and Morin 2023; Durand et al. 2009), the Rockies (Tarek et al. 2020), and HMA (Khanal et al. 2023; An et al. 2017; Madhura et al. 2015; Krishnan et al. 2019). However, global reanalysis datasets have a relatively coarse spatial resolution of 30–50 km, and their data assimilation systems often exclude in situ observations in mountain regions (ECMWF 2021). Consequently, reanalysis products can struggle to capture the small-scale spatiotemporal variability of snowfall that characterizes mountainous regions, especially extremes (Bannister et al. 2019; Khanal et al. 2023; Potter et al. 2023). One approach to tackle this issue has therefore been to dynamically downscale reanalysis datasets using a regional climate model (RCM) to generate high-resolution gridded precipitation products (Potter et al. 2023; Ménégoz et al. 2013; Wang et al. 2021; Norris et al. 2020; Bannister et al. 2019; Maussion et al. 2011). In such approaches, the RCMs are typically run at spatial resolutions between 1 and 10 km to better represent the critical multiscale interactions between atmospheric flows and complex/steep topographical features that influence snowfall, and especially extremes (Collier and Immerzeel 2015; Potter et al. 2018; Orr et al. 2017). However, comprehensive assessments of snowfall amounts simulated by RCMs in mountainous regions are currently lacking due to the aforementioned concerns over the sparseness and quality of snowfall measurements.

These challenges highlight the urgent need for improved and targeted methodologies to accurately quantify snowfall in mountainous areas. To address this issue, Pritchard et al. (2021) developed an innovative method for measuring snowfall on mountain lakes during sustained freezing conditions, when the catchment is frozen, and no runoff enters the lake (from either snowmelt or rain falling on the snowpack and refreezing). Under these no-runoff conditions, winter precipitation (snow, rain, ice, or graupel, hereafter termed "snowfall" when referring to such observations) falling onto the lake surface produces an instantaneous change in water pressure which can be measured with high accuracy using a water pressure sensor placed at the bottom of the lake. The pressure change corresponds directly to the water content of the precipitation averaged over the whole lake surface. This method is conceptually similar to a snow pillow but can be applied on the much larger spatial scale of lakes in the mountain landscape (from hundreds of meters to kilometers) and therefore is particularly well suited to testing and constraining snowfall output from high-resolution RCMs which have grid cells on a similar scale (Pritchard et al. 2021).

Another concern related to RCMs is, however, their uncertain representation of the microphysical properties of clouds and precipitation, especially snowfall (Morrison and Milbrandt 2015; Orr et al. 2017). Large-scale snowfall in RCMs is modeled using a parameterization of ice-phase microphysics that governs the growth and fallout of ice and snow particles (Orr et al. 2017; Garvert et al. 2005; Alcott and Steenburgh 2013), and a long-standing issue with ice-phase microphysics schemes is their high sensitivity to the choice of process rate parameter values (Chandra et al. 2020; Morrison and Milbrandt 2015). Many of these remain poorly understood and constrained due to limited in situ snowfall observations (Lin et al. 1983; Schoenberg Ferrier 1994; Thompson et al. 2008; Milbrandt and Yau 2005; Morrison et al. 2009; Listowski and Lachlan-Cope 2017). For example, these schemes are particularly sensitive to the choice of parameter values controlling the fall speeds for ice and snow, which are highly uncertain (Morrison and Milbrandt 2015; Gumber et al. 2024). Better representation of ice and snowfall speeds in simulations is particularly important for improving the spatial distribution of snowfall (including precipitation lapse rates), as this controls how far they are advected downwind as they fall through the atmosphere before settling on the surface (Jensen et al. 2020; Sterzinger and Igel 2021; Colle and Zeng 2004). Recent advances in imaging technology have enabled studies to better report the fall speeds of frozen hydrometeor particles, suggesting that fall speed could be explored as a method for tuning the spatiotemporal representation of snowfall in RCMs (Vázquez-Martín et al. 2021; Garrett et al. 2012; Takasuka et al. 2024).

In this study, we aim to use new lake-based snowfall observations from six sites located in the west–central Himalayas, European Alps, and central Rockies to assess the representation of snowfall simulated by the ERA5-driven atmosphere-only Met Office Unified Model (MetUM) at a grid spacing of 1.5 km. These three target regions provide a wide range of orographic features and snowfall regimes, enabling model evaluation across diverse conditions. The snowfall output from the MetUM is additionally fine tuned by adjusting the fall speed of snow particles so that it is best able to capture the observed snowfall amounts, especially for extreme events. We also compare snowfall characteristics from radars with those from the model, as these are useful for capturing a three-dimensional representation of precipitation. We subsequently use hydrometeor output from our model to examine the microphysical conditions related to extreme snowfall for the three study regions.

2. Data, model, and methods

a. Data

The six lake-based snowfall measurement sites used in this investigation include two sites in the Alps (Tomasee and Rofental), three in the west–central Himalayas (Ghepan, Hampta, and Mugu), and one in the central Rockies (Flowing Park; Fig. 1). The Tomasee and Mugu lakes sit in alpine cirques, Rofental sits in a high alpine valley, Hampta sits on a mountain promontory, and Flowing Park sits on a plateau. Ghepan sits in a relatively large and deeply incised glacierized trough surrounded by peaks that are 2000–4000 m higher than the valley floor. A summary of the details of each site is listed in Table 1. The length of the six lakes ranges from 0.30 to 2.3 km, with an average of 1.3 km, similar to the 1.5-km grid spacing of our MetUM.

In each case, we installed commercial, high-precision water pressure sensors (with a nominal precision of 0.1% of full scale) on the lakebed, before the winter freeze up. To achieve optimal measurement sensitivity, gauges were positioned in shallow water depths of 1–5 m and configured with a relatively narrow operating pressure of 1–10 bar. All six lakes froze over completely during the monitoring periods. The instruments continuously measured water pressure and temperature and were also equipped with breather tubes for natural ventilation (open to the air at the logger box) to correct for atmospheric pressure fluctuations. A ground-level thermistor was also installed to record snow-base temperatures, allowing us to mark the onset of snowmelt runoff in the subsequent melt season/spring. Each logger was powered by a 12-V lead–acid battery. Data from each measurement site were collected for a single winter season, beginning when the associated lake catchment first freezes in early winter and ending when snow begins to thaw in spring, a period of around 6 months. The time series of water pressure signals from the various sites, sampled at 10-min intervals, typically show decreasing lake levels over the winter season due to net drainage out of the lakes, punctuated by abrupt jumps in pressure on hourly to daily time scales associated with snowfall events (see Fig. S1 in the online supplemental material). These pressure signals were processed to calculate the associated SWE at a temporal resolution of 3 h (after Pritchard et al. 2021).

Uncertainties in estimating SWE can also arise from several sources, including instrumental uncertainty in the pressure measurements and in the magnitude of the lake-drainage signal. In addition to these site-specific challenges, all locations

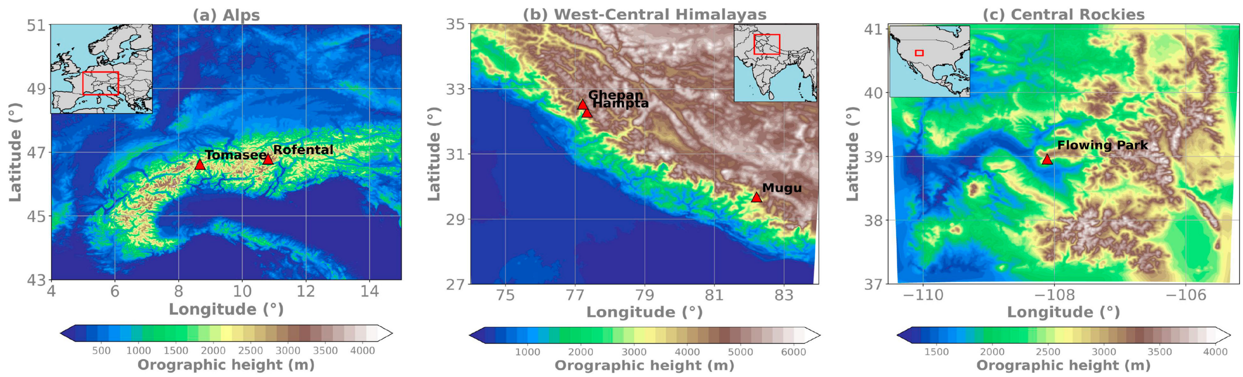

FIG. 1. Maps showing MetUM domains and orography (m; shading) at 1.5-km grid spacing for the (a) Alps, (b) west–central Himalayas, and (c) central Rockies, with the positions of the lake-based snowfall measurement sites indicated by red triangles. Note that the orography in each of the panels has different ranges.

were subject to a baseline measurement uncertainty arising from the precision limits of the pressure gauge. The relative instrumental uncertainty was determined from pressure measurements collected at constant water depth in a laboratory over a 1-h interval, following Pritchard et al. (2021). Because our pressure sensor automatically compensates for nonlinear sensitivity and temperature dependencies, we treat this instrumental uncertainty as constant. Drainage uncertainty arises from uncertainty in the linear fits to the pressure data before and after the snowfall event. These various sources of uncertainty were quantified from the pressure time series (such as in Fig. S1) and estimated at the end of each event as in Pritchard et al. (2021) (see Table S1).

After applying a minimum threshold of 1 mm water equivalent (i.e., 1 kg m^{-2}) for the total precipitation over each observed snowfall event, the resulting measurements at Mugu, Tomasee, Hampta, Flowing Park, and Rofental have relatively small uncertainties, averaging 4%, 5%, 6%, 7%, and 9% of the event totals, respectively, with somewhat greater uncertainty (18%) for Ghepan. These higher uncertainties at Ghepan can be attributed to the lake's larger area and hence greater exposure to wind, which can generate swelling and create transient air pressure anomalies, and a small number of snowfall events were also excluded due to contamination by water pressure signals from glacier calving events or avalanches (Pritchard et al. 2021).

We also utilize gridded datasets of radar reflectivity over the Alps and central Rockies, which allows us to evaluate the spatial representation of snowfall in the MetUM on regional scales, i.e., in contrast to the localized lake-based measurements. In these datasets, moderate snowfall is typically associated with reflectivity values in the range of 10–30 dB*Z*, while higher reflectivity values of 30–40 dB*Z* may indicate more intense snowfall with larger aggregates. For the Alps, we use a dataset of maximum reflectivity composites produced from the European Operational Program for Exchange of Weather Radar Information (OPERA) network (Saltikoff et al. 2019). This dataset has a grid spacing of 2 km × 2 km and includes data from around 200 operational radars. For the central Rockies, we use a dataset of base reflectivity for the contiguous United States produced from Next Generation Weather Radar (NEXRAD) mosaics from the Iowa Environmental Mesonet (Iowa State University, 2024). This dataset has a grid spacing of 2 km × 2 km and is generated by combining information from over 130 individual radars. Note that one limitation of radar reflectivity datasets in complex terrain is that they are affected by beam blockage. In both datasets, (i) reflectivity estimated from partially blocked sectors (up to

TABLE 1. Overview of the six lake-based snowfall measurement sites, including their location, latitude and longitude of the pressure sensor location, altitude and size of the lakes, selected observation period, and the number of snowfall events recorded.

Location of the site	Latitude (°) and longitude (°)	Altitude (m), effective lake length (km)	Observation period	No. of snowfall events
Tomasee, Alps	46.63, 8.67	2340, 0.30	1 Jan–20 Mar 2019	14
Rofental, Alps	46.79, 10.81	2730, 0.36	30 Oct 2023–14 Feb 2024	28
Hampta, west–central Himalayas	32.28, 77.34	4600, 0.33	2 Nov 2021–14 Mar 2022	22
Ghepan, west–central Himalayas	32.53, 77.22	4102, 2.26	2 Nov 2021–14 Mar 2022	24
Mugu, central Himalayas	29.68, 82.21	4089, 0.50	13 Oct 2023–15 Feb 2024	5
Flowing Park, central Rockies	38.96, −108.11	3062, 0.90	2 Nov 2023–1 Apr 2024	18

70%) are bias corrected and retained in the composites but prescribed reduced weighting compared with unblocked sectors, and (ii) data from sectors with blockage percentages exceeding 70% are discarded and are not used for compositing. This procedure substantially enhances the azimuthal uniformity of reflectivity fields and allows data from neighboring radars to fill the gaps for sectors with >70% obstruction. Additionally, an equivalent gridded radar reflectivity dataset for the Himalayas is not publicly available.

Finally, we assess snowfall-related systematic biases in ERA5 reanalysis, which provides data from 1940 to the present, by comparing with the lake-based snowfall observations and model simulations. It represents four cloud species (cloud liquid, rain, ice, and snow) that are described prognostically by the precipitation scheme (Hersbach et al. 2020). For this, we retrieved ERA5 3-hourly snowfall data on a 0.25° × 0.25° grid for the same periods as the lake-based measurements.

b. *Atmospheric model*

We use version 13.0 of the kilometer-scale regional configuration of the MetUM. The science configuration of the dynamics and physics schemes used by the model is the Regional Atmosphere and Land, version 3 (RAL3; Bush et al. 2025). This uses a dynamical core that solves nonhydrostatic, fully compressible mass and momentum equations applied to a deep atmosphere (Wood et al. 2014). A scale-aware, nonlocal, one-dimensional boundary layer scheme is employed to resolve turbulence-induced vertical mixing (Lock et al. 2000; Boutle et al. 2014). The radiation parameterization used is the Edwards–Slingo scheme, which employs a flexible radiative transfer model that handles the radiative impact of cloud water, total ice, and snow (Edwards and Slingo 1996). Parameterized convection is switched off, as with a grid spacing of 1.5 km, the convection is resolved explicitly (Honnert et al. 2021). However, we note that a grid spacing of 1.5 km does not imply that the flow features over the lakes are fully resolved, as the effective resolution of the model is several times the grid spacing (Abdalla et al. 2013). Representation of the orography in the model is derived from the Shuttle Radar Topography Mission (SRTM) dataset at a grid spacing of 100 m (Farr et al. 2007).

The physics schemes used also include a bimodal cloud fraction scheme (Van Weverberg et al. 2021) and the double-moment cloud microphysics scheme Cloud Aerosol Interaction Microphysics (CASIM; Field et al. 2023), which includes five different hydrometeor species (cloud liquid, rain, ice, snow, and graupel). The particle size distribution (PSD) for each hydrometeor species is modeled using a generalized gamma function with a fixed shape parameter. In the double-moment CASIM configuration, the hydrometeor mass/mixing ratio and number are sedimented separately using their respective weighted fall speeds, enabling the smaller more numerous particles to get separated from the fewer larger particles. The terminal velocity $V_x(D)$ of a hydrometer species x in CASIM is represented as

$$V_x(D) = a_x D^{b_x}\left(\frac{\rho_o}{\rho}\right)^{f_x}, \tag{1}$$

where D is the particle diameter; ρ and ρ_o are the respective densities of air at the model level and the surface; and a_x, b_x, and f_x are empirically derived parameters. For snow particles, these parameter values are prescribed as $a_x = 12$, $b_x = 0.5$, and $f_x = 0.5$ (Field et al. 2023). This configuration of the MetUM (that uses CASIM's default parameter settings for the fall speed of snow particles) is labeled CTRL.

The model is set up over three domains with grid spacings of 1.5 km, positioned over the Alps (comprising 650 × 650 grid points), west–central Himalayas (650 × 650 grid points), and the central Rockies (300 × 300 grid points; see Fig. 1). These domains include 70 vertical levels between the surface and a model top at 40 km, with 16 levels within the lowest 1000 m of the atmosphere. The model simulations for each of the three domains consist of a series of 36 hourly forecasts, with outputs saved from $T + 12$ to $T + 36$ h and the initial 12 h of the forecast discarded as spinup [i.e., following the methodology of Orr et al. (2023)]. Initial and boundary conditions for the three domains are provided by the global configuration of the MetUM at N768 resolution (equivalent to around 17-km grid spacing), which is initialized at its surface and lateral boundaries by ERA5 reanalysis data with a grid spacing of 0.5°. The global model uses the Global Atmosphere 6.0 (GA6.0) science configuration (Walters et al. 2019). Note that we also exclude the influence of the relaxation zone along the domain margins, as the coarser resolution spins from 17 to 1.5 km. As the model outputs are compared with observations at central points within the domain, this approach ensures that any impact on the results is minimal and unlikely to be significant.

The outputs for each domain are at 3-hourly temporal resolution and include accumulated snowfall, instantaneous maximum radar reflectivity produced from all hydrometeor types, instantaneous mixing ratios for each hydrometeor type on model levels, and instantaneous temperature on model levels.

c. *Methodology*

Five model sensitivity experiments were designed to investigate the sensitivity of snowfall to key microphysical parameters, in addition to the default CTRL simulation (summarized in Table S2). Because liquid water formation is susceptible to microphysical processes governing the rate of ice crystal formation and growth due to the Wegener–Bergeron–Findeisen process (Price et al. 2025 and references therein), the first two sensitivity experiments perturb the cloud drop size distribution (DSD) within CASIM to test the effects of droplet activation on the simulated cloud microphysics. In the experiment labeled i) DSD_MICROPHYS_1, we increased the prescribed droplet number concentration from 150 to 550 cm^{-3} and slightly narrowed the fixed hydrometeor spectral widths, and in (ii) DSD_MICROPHYS_2, we lowered the droplet number concentration from 150 to 50 cm^{-3}, while keeping all other model settings identical to CTRL.

A further three sensitivity experiments use the improved understanding of the fall speeds of frozen hydrometeor particles (Vázquez-Martín et al. 2021; Garrett et al. 2012; Takasuka et al. 2024) to investigate the sensitivity of snowfall/SWE on the ground simulated by the MetUM to the parameter values for the fall speed of snow particles used by CASIM [Eq. (1)], i.e., how this affects the sedimentation dynamics of falling snow. Published values of snow terminal velocities (Vázquez-Martín et al. 2021; Khvorostyanov and Curry 2002; Kuhn and Gultepe 2016) indicate that fall speed variability allows for a range of fall speed factors (FSF) a_x between 4 and 16, with the other existing exponent values as in Field et al. (2023), i.e., encompassing the full spectrum of observed fall speed values. This variability in values is detected because frozen clouds contain an assortment of crystal types, ranging from the smallest snow spheres ($D \sim 0.06$ mm) to the larger needles, columns, and graupel particles ($D \sim 3$ mm), with their terminal velocities varying from 0.06 to 1.6 m s^{-1} (Vázquez-Martín et al. 2021; Kajikawa 1973). Therefore, to examine how this variability influences the sedimentation dynamics of falling snow, experiments FSF_MICROPHYS_3, FSF_MICROPHYS_4, and FSF_MICROPHYS_5 reduce the value of a_x in the CASIM microphysics scheme from 12 to 10, 8, and 4, respectively, while keeping all other model settings identical to CTRL. This effectively generates slower fall speeds of snow particles compared to CTRL, which should result in them being advected further downwind in EXP and affecting the distribution of accumulation (Colle and Zeng 2004; Sterzinger and Igel 2021).

All test configurations were used to simulate an extreme snowfall event that occurred at Tomasee from 2100 UTC 12 January 2019 to 2300 UTC 14 January 2019, and the results were compared with the available lake-based observations (Fig. S2). The results show that the experiments that modified the snow FSF have a much stronger influence on total snowfall than the experiments modifying DSD. For example, a moderate reduction in fall speed (as in FSF_MICROPHYS_4) improves model–observation agreement, whereas excessive reduction (as in FSF_MICROPHYS_5) leads to severe underestimation. These sensitivity tests identified FSF_MICROPHYS_4 (i.e., $a_x = 8$) as the configuration that showed the best agreement with the observed snowfall amounts (Fig. S2). Hereafter, this configuration is referred to as EXP and, together with CTRL, is selected as the focus of the analysis in the results section.

The CTRL and EXP models are subsequently ran for the same period as the available observations (see Table 1). Modeled snowfall values are subsequently used to create a time series of 3-hourly accumulated SWE for each site. As it is uncertain that the lake is well aligned within a single model grid cell, these values are computed by linearly interpolating model output from the four surrounding grid points, ensuring that the model values better represent the local snowfall characteristics averaged across a larger region. The modeled snowfall output is then postprocessed to remove small events using the same threshold applied to observations. Finally, the observed snowfall time series is used to identify and select snowfall events in the model, determining the onset, duration, and event-accumulated SWE for each event at each of the six sites. This allows for a direct event-by-event comparison of snowfall events between the observations and simulated snowfall events. A similar time series of snowfall SWE is produced for ERA5 data at each site, with the data retrieved using the nearest-neighbor approach. The CTRL, EXP, and ERA5 time series are subsequently compared with the lake-based time series.

We qualitatively compare radar-observed and model-derived reflectivity contours to identify model biases in the regional representation of precipitation over the Alps and the central Rockies. For the Alps, this is done by comparing values of maximum radar reflectivity from the OPERA RADAR dataset against model-derived values for two winter case studies (1800 UTC 12 January 2019 and 1800 UTC 1 December 2023). For the central Rockies, we compare values of base reflectivity against the Iowa Environmental Mesonet dataset against model-derived values for two winter cases (1200 UTC 2 February 2024 and 1200 UTC 16 November 2023). All four case studies consisted of heavy snowfall across the Alps and central Rockies, respectively. However, it is important to note that model-derived radar reflectivity can exhibit relatively large biases because this approach requires making assumptions about the hydrometeor properties (Heymsfield et al. 2023). In particular, as model-based reflectivity estimates are derived from a higher moment of the assumed PSD, they are highly dependent on the scattering characteristics of the hydrometeors, which are difficult to ascertain from either surface or airborne measurements (Westbrook et al. 2006). For example, the model-derived snowfall reflectivity is the integral over the size distribution of the fourth power of the snow particle diameter, making it highly sensitive to assumptions about poorly constrained microphysical details such as in-cloud crystal size, orientation, habit, and density (Kou et al. 2023; Miltenberger et al. 2018). Note that radar-observed and model-based reflectivity values below 0 dBZ are not considered as these correspond to weak radar echoes mainly caused by background noise/clutter rather than actual precipitation.

Finally, we also examine instantaneous hydrometeor mixing ratios calculated by the MetUM to investigate the microphysical conditions related to extreme snowfall for each of the three regions studied. We focus on three such events at 1800 UTC 13 January 2019, 1800 UTC 4 January 2022, and 0600 UTC 2 February 2024, respectively, over the Alps, the west–central Himalayas, and the central Rockies.

3. Results

a. *Precipitation*

Figure 2 compares the measured total snowfall amounts for all the individual events observed at the six sites with corresponding estimates from the CTRL and EXP simulations. The number of events used from each site is given in Table 1, with a combined number of 111 events examined over all six sites (with Table S1 giving the actual measured amounts and uncertainties for each of them). The measurements show that the total snowfall amounts of the observed events varies from 1 kg m^{-2} (i.e., the detection threshold) to up to 200 kg m^{-2}, i.e., capturing a range of snowfall amounts from small events to large events. Comparison of the simulated values with the measured snowfall values for Tomasee, Rofental, Ghepan, and Hampta (Figs. 2a–d) shows a small systematic overestimation in the 10–200 kg m^{-2} range, although the bias is reduced for EXP compared to CTRL, quite evidently over

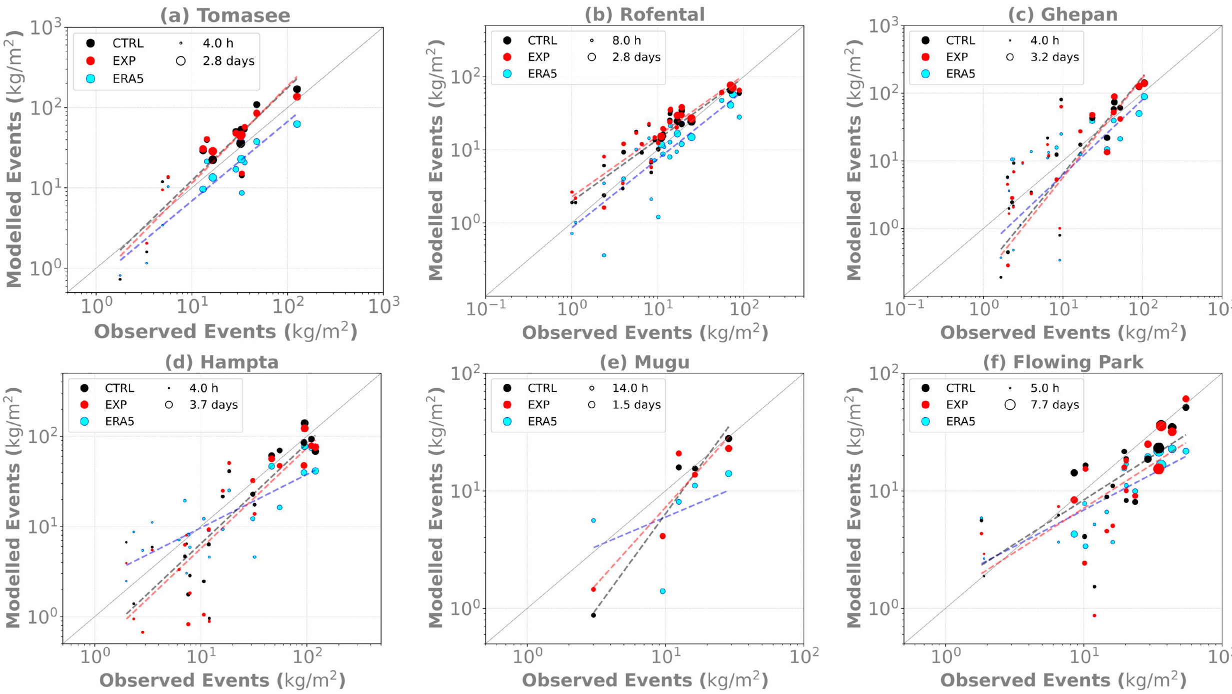

FIG. 2. Scatterplots of observed vs modeled snowfall totals (kg m^{-2}) for all events at (a) Tomasee, (b) Rofental, (c) Ghepan, (d) Hampta, (e) Mugu, and (f) Flowing Park. The modeled outputs are from the CTRL (black) and EXP (red) simulations. Equivalent snowfall totals from ERA5 are also shown (cyan). Event durations are estimated from the observed lake water pressure data at a temporal resolution of 10 min and are represented by the size of the filled circles, with the range of durations varying by location, indicated by the smallest and largest circles for each site. The number of snowfall events for each location is listed in Table 1. Events are identified only if total snowfall amount exceeds 1 kg m^{-2} for each event. The dashed lines represent lines of best fit.

Tomasee. This is therefore consistent with the EXP simulation, reducing the intensity of snowfall over some sites by redistributing more of it further downstream (see Fig. S3). The comparison of measured and simulated values for low snowfall events (<20 kg m^{-2}) at Ghepan and Hampta tends to be rather scattered. By contrast, the simulated snowfall amounts at Flowing Park (Fig. 2f) tend to underestimate the measured values for smaller events.

To further investigate the comparison of the simulated and measured snowfall values, Fig. 3 compares histograms of 3-hourly snowfall accumulation from the measured snowfall amounts observed for the six sites with the values from the CTRL and EXP simulations. Figure 3 aligns with the results shown in Fig. 2, confirming that the EXP simulation generally results in a reduction in extreme snowfall amounts compared to CTRL (without any noticeable change in the onset and end times of events between CTRL and EXP) and a better agreement with measured values, especially for Tomasee, Ghepan, Hampta, and Mugu (Figs. 3a,c–e). Although the results for Ghepan and Hampta show that both CTRL and EXP tend to overestimate higher snowfall amounts, the results are comparatively better for EXP. Figure 3 also confirms that, for Rofental (Fig. 3b), both CTRL and EXP distributions slightly underestimate the right-hand side of the measured distribution, although EXP yields slightly higher snowfall amounts on the tail end and agrees well with the observed values. It is further noted from Figs. 2 and 3 that Tomasee, Rofental, Ghepan, and Hampta received more snowfall than other sites, sometimes in excess of 100 kg m^{-2} for each event, with their 3-hourly accumulations in the 10–20 kg m^{-2} range.

Figure 4 uses Taylor diagrams to provide a concise statistical summary of the differences between the simulated and observed snowfall, which show correlation, normalized standard deviation, and root-mean-square error (RMSE). The results show that the standard deviation for EXP is closer to a value of one at Tomasee, Rofental, Mugu, and Flowing Park compared to CTRL (Figs. 4a,b,e,f), indicating that EXP is characterized by greater precision in snowfall variability at these sites. However, the results also show that the correlation for EXP compared to CTRL is slightly higher for Tomasee, similar for Rofental, Ghepan, and Hampta, and lower for Mugu and Flowing Park. Over Ghepan, both model versions perform similarly (Fig. 4c). In terms of RMSE, the results for EXP and CTRL are similar for Rofental, Ghepan, Hampta, and Flowing Park, with only Tomasee showing a reduction in RMSE in EXP compared to CTRL.

Figure 5 shows the upper-tail percentiles (80th–100th) of cumulative snowfall (kg m^{-2}) for observed and modeled snowfall events, along with the associated bias (kg m^{-2}), aggregated across all the sites. Across percentile thresholds from the 80th to the upper extreme values, consistent differences emerge between EXP and CTRL. EXP exhibits an improvement

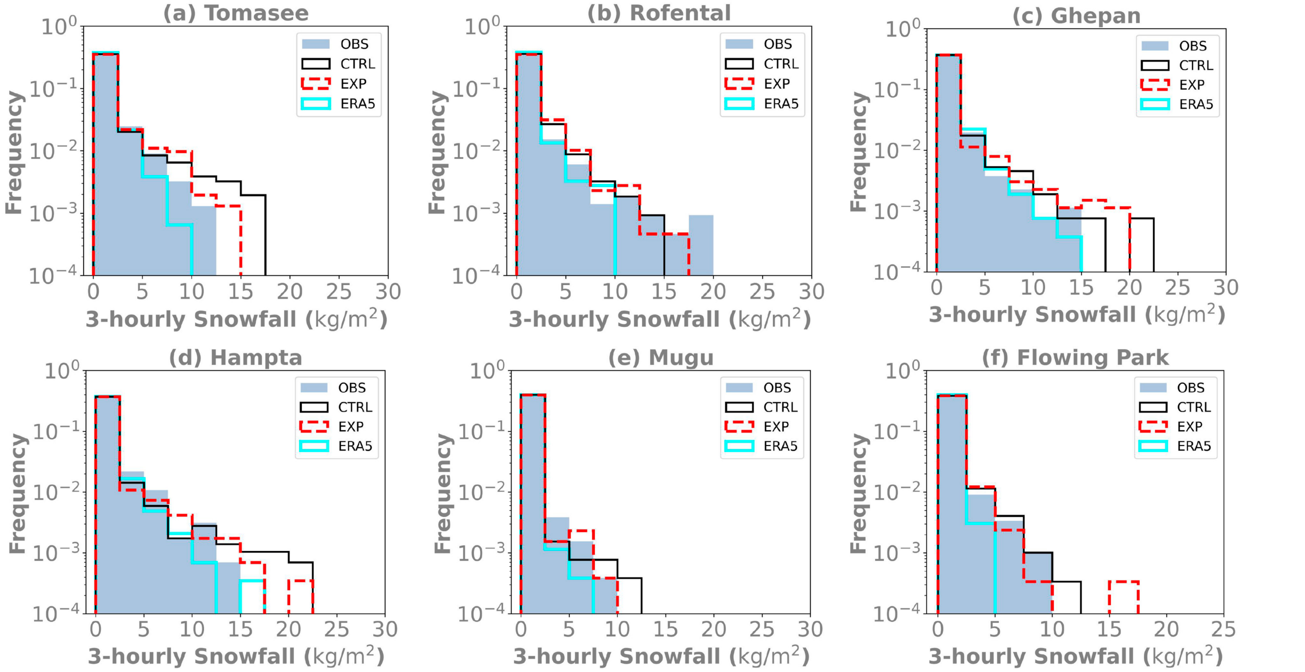

FIG. 3. Histograms of observed and modeled 3-hourly accumulated snowfall (kg m^{-2}) for all events at (a) Tomasee, (b) Rofental, (c) Ghepan, (d) Hampta, (e) Mugu, and (f) Flowing Park. The modeled outputs are from the CTRL (black) and EXP (red) simulations. Equivalent snowfall totals from ERA5 are also shown (cyan).

to the distribution of high-tail events (Fig. 5a), with snowfall amounts more closely aligned with observations across most percentile thresholds (Fig. 5b), and lower bias than CTRL (Fig. 5c). In contrast, CTRL shows a slightly higher correlation (see Fig. S4b), but it tends to overestimate snowfall extremes, particularly at higher percentiles.

Figure 6 compares the time series of measured snowfall amounts at Tomasee, Hampta, and Flowing Park (i.e., representing each of the three target regions) with estimates from the CTRL and EXP simulations. Throughout the winter seasons, all sites experienced multiple snowfall events, typically lasting from a few hours to a few days. The results show that the simulations are able to capture the timing of the beginning and cessation of the snowfall events accurately with the overall onset bias for both CTRL and EXP ranging from −6 to 3 h and an RMSE value of 8.16 h. However, CTRL again typically tends to overestimate the snowfall amounts for moderate to large events, while this bias is reduced in EXP.

At Tomasee (Figs. 6a,b), the time series includes a notable extreme event from 13 to 15 January, which is associated with large quantities of snowfall along the northern slopes of the Alps occurring in response to the forced uplift of strong moisture-laden northwesterly winds, with values of simulated integrated vapor transport reaching up to 350 kg m s^{-1} (not shown). During this event, the snowfall amount simulated in CTRL reached a peak value of 16 kg m^{-2} in a 3-h period, which is reduced to 12 kg m^{-2} over this period in EXP, in better agreement with the observations. Moreover, analysis of the event total for this period shows that the snowfall amount is reduced by 19% for EXP (136.4 kg m^{-2}) compared to CTRL (169.2 kg m^{-2}), aligning more closely with the observed amount of 125.6 kg m^{-2}.

At Tomasee, such longer duration events (~3 days) accounted for over 34% of the total received snowfall for the season examined, i.e., making a substantial contribution to the seasonal total. By contrast, the other smaller/short-duration events—the shortest only around 3 h in duration—observed at Tomasee were mainly driven by localized microphysical processes with the dynamics driven typically by either westerlies or southerlies (not shown). Even during these cases, for example, the events in March, the snowfall amounts show a reduction in EXP compared to CTRL and a better match with observations. This is also consistent with EXP typically reducing snowfall accumulation at certain sites and redistributing more of it further downstream. For example, EXP redistributed more of the snowfall further downstream over the Alps compared to CTRL for the period from 0000 UTC 13 January 2019 to 2300 UTC 15 January 2019 (Fig. S3a), which resulted in EXP values reducing over Tomasee and closer to the observed values (Fig. 6b). By contrast, Rofental experienced a net increase in snowfall in EXP relative to CTRL for the period from 0000 UTC 30 October 2023 to 2300 UTC 31 October 2023, which also moved the EXP values closer to the observed values compared to CTRL (not shown).

At Hampta (Figs. 6c,d), the time series again shows a similar reduction in snowfall amount in EXP compared to CTRL. Here, the EXP and CTRL simulations underestimate the observed cumulative seasonal totals by 16% and 6%, respectively. The time series for Hampta includes a number of extreme events in January, associated with large quantities of

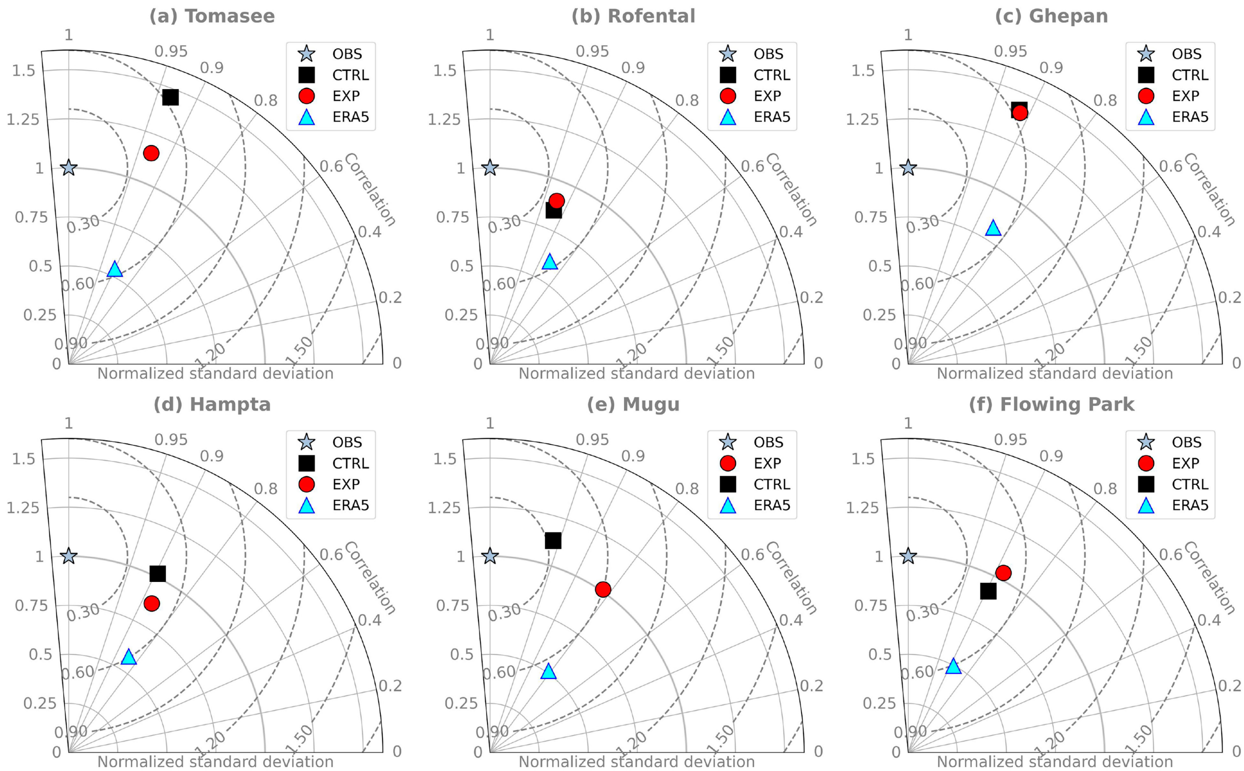

FIG. 4. Taylor diagrams of observed vs modeled snowfall at (a) Tomasee, (b) Rofental, (c) Ghepan, (d) Hampta, (e) Mugu, and (f) Flowing Park. The modeled outputs are from the CTRL (black) and EXP (red) simulations. Equivalent snowfall results from ERA5 are also shown (cyan). Radial distance indicates the normalized standard deviation (variability), azimuthal sectors represent the correlation coefficient, and concentric dashed contours centered on OBS denote the RMSE (kg m^{-2}).

snowfall along the western slopes of the Himalayas (not shown). These events together contributed around 350 kg m^{-2} of snowfall, accounting for nearly 50% of the cumulative seasonal total. These extreme snowfall events are in response to the forced uplift of strong moisture-laden northwesterly winds associated with a deep cyclonic system (not shown). This synoptic setup is a characteristic feature of western disturbances, the dominant winter weather systems influencing the western Himalayas (Dimri et al. 2015; Hunt et al. 2025; Bharati et al. 2025).

At Flowing Park (Figs. 6e,f), the time series shows that the majority of its snowfall came from a number of major events in February and March (44% of the total events in the 2 months combined), which accounted for 46% of the cumulative seasonal total. These results show only a marginal difference between the CTRL and EXP simulations, with both underestimating the seasonal snowfall amounts by 20% and 25%, respectively. However, while cumulative snowfall is a useful diagnostic of seasonal accumulation because it integrates snowfall over several months, it can amplify intensity errors. For example, the big snowfall event

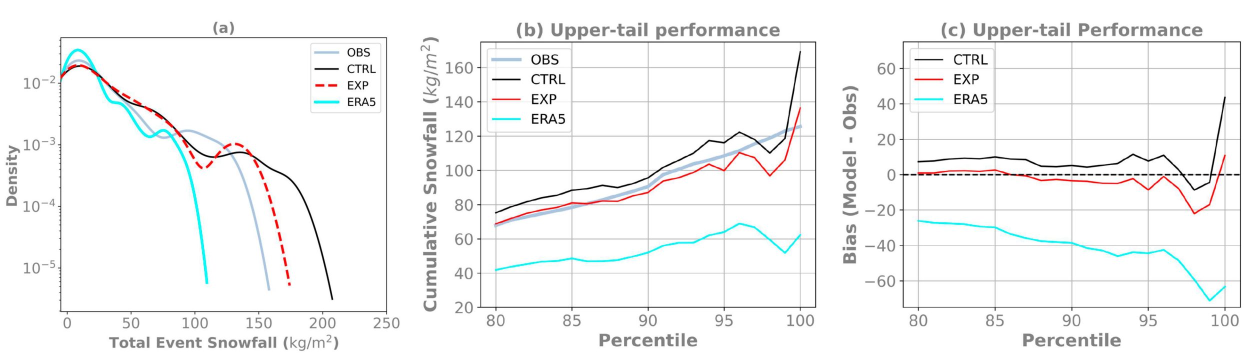

FIG. 5. (a) Comparison of density functions of observed and modeled snowfall. (b) Upper-tail percentiles (80th–100th) of cumulative snowfall (kg m^{-2}) for observed and modeled snowfall events. (c) Upper-tail bias between observed and modeled snowfall events. Modeled outputs are from the CTRL (black) and EXP (red) simulations. Equivalent snowfall from ERA5 is also shown (cyan).

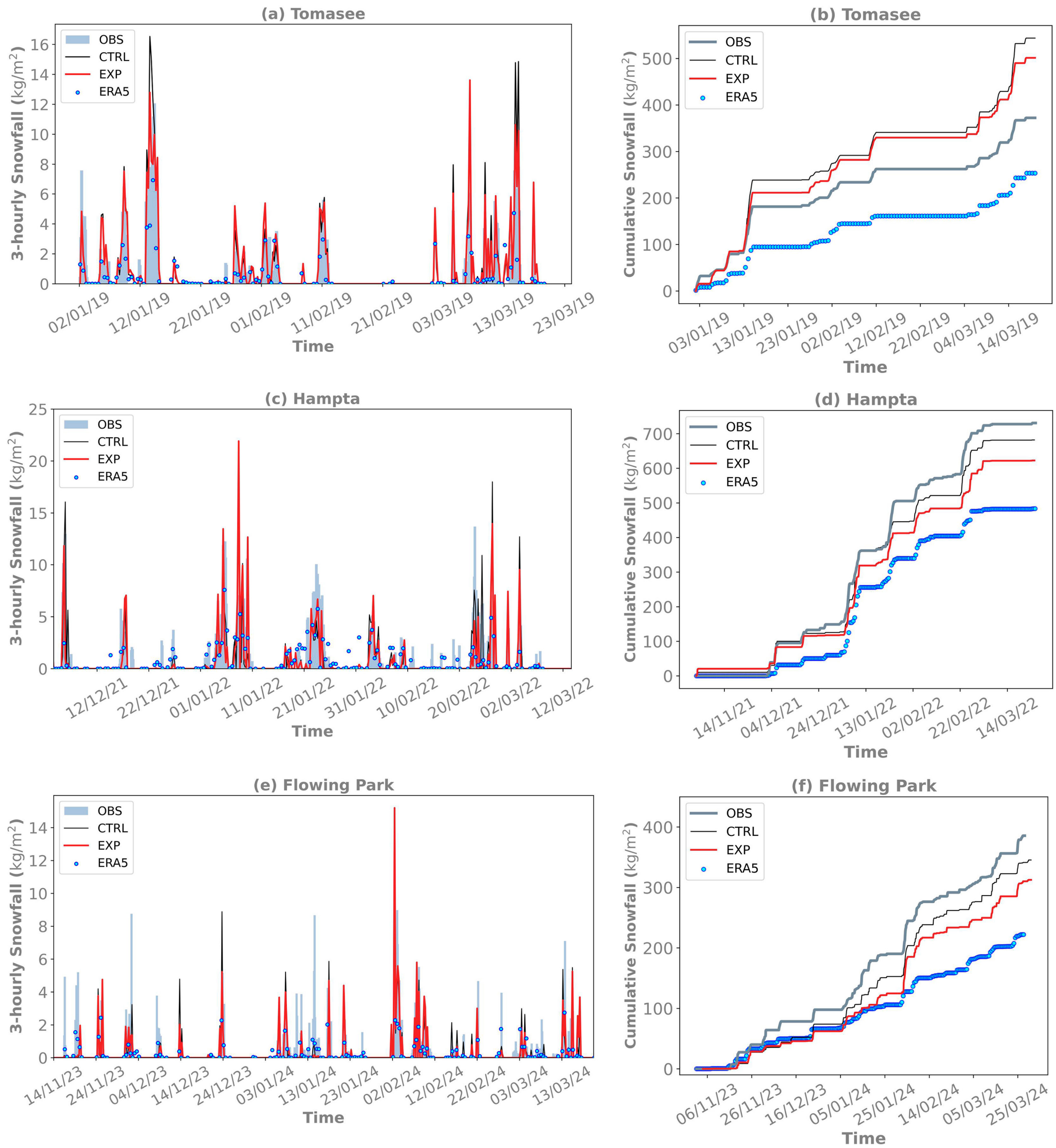

FIG. 6. Time series of observed and modeled (a),(c),(e) 3-hourly and (b),(d),(f) seasonal cumulative snowfall (kg m^{-2}) at (a),(b) Tomasee, (c),(d) Hampta, and (e),(f) Flowing Park. The modeled outputs are from the CTRL (black) and EXP (red) simulations. The results for Tomasee are for the period 1 Jan 2019–20 Mar 2019, Hampta for 2 Nov 2021–14 Mar 2022, and Flowing Park for 2 Nov 2023–1 Apr 2024. Equivalent snowfall totals from ERA5 are also shown (cyan).

between 24 December 2021 and 13 January 2022 over Hampta (Fig. 6d) is overestimated in CTRL relative to EXP with the errors persisting over the remainder of the winter season. As a result, snowfall accumulation in CTRL may appear closer to observations for compensating reasons, even though extremes are better captured in EXP.

In addition, we also examined aggregated results for all 111 snowfall events over the six sites (Fig. S4 and Fig. 5a) that, in general, agree with the results from the individual sites that EXP modestly improves snowfall relative to CTRL. In particular, they show that, for all events combined, (i) EXP has a better representation of the upper tail of the snowfall distribution, consistent with it improving the representation of extreme events; (ii) the overall snowfall bias for EXP is 2.62 kg m^{-2}, which is lower than the bias of 3.65 kg m^{-2} for CTRL (Fig. S4a); and (iii) the RMSE value for EXP is 15.16 kg m^{-2}, which is lower than 15.94 kg m^{-2} for CTRL—although both are less than 1% of the total snowfall amount.

Figures 2–6 and Fig. S4 also show that ERA5 systematically underestimates snowfall amounts at all sites. For example, the cumulative seasonal snowfall amount from ERA5 at Tomasee, Hampta, and Flowing Park is underestimated by 33%, 37%, and 46%, respectively (Fig. 6). Additionally, the estimated RMSE value for all 111 snowfall events across all the six sites

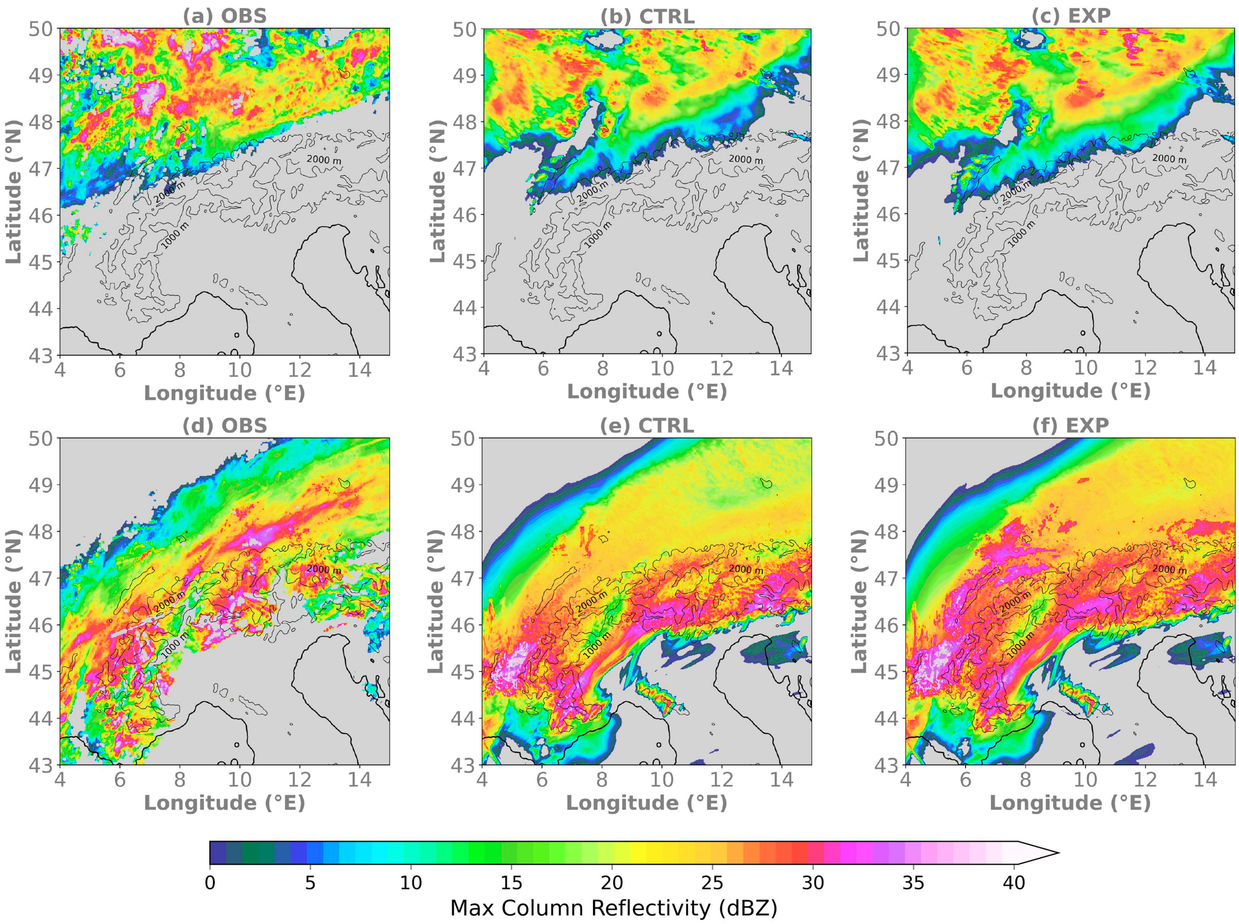

FIG. 7. Comparison of observed and modeled maximum radar reflectivity (dBZ; shading) for the Alps at (a)–(c) 1800 UTC 12 Jan 2019 and (d)–(f) 1800 UTC 1 Dec 2023. The modeled outputs are from the CTRL and EXP simulations. Also shown are the model orography (m; contours).

is 17.26 kg m^{-2}, which is higher than both the estimates for EXP and CTRL (Fig. S4). Moreover, the corresponding overall bias for ERA5 is −6.75 kg m^{-2}, which again is much higher than the model estimates (Fig. S4). Finally, ERA5 snowfall shows a significant negative bias in the upper-tail percentile range, indicating poor performance in capturing both magnitude and distribution of snowfall extremes (Fig. 5). The comparatively poor performance of ERA5 snowfall is likely partly linked to its relatively coarse 0.25° resolution and consequent increased smoothing of its orography over the three target regions (see Fig. 10), which can lead to a more even distribution of precipitation compared to reality due to reduced orographic effects (Webster et al. 2008; Gilbert et al. 2025). Additionally, convection is also parameterized in ERA5, which could impact moisture partitioning, yielding lower snowfall totals than the MetUM simulations that explicitly resolve convection at 1.5-km resolution (Taszarek et al. 2021; Gilbert et al. 2025; Orr et al. 2017).

b. Radar reflectivity

Figure 7 compares the observed maximum radar reflectivity composite with the maximum column reflectivity (dBZ) from both the CTRL and EXP simulations for the two snowfall events over the Alps. The event at 1800 UTC 12 January 2019 involves northwesterly flow colliding with the Alps, resulting in heavy snowfall extending over much of its northern flank. For this event, the radar observations show significant spatial variability in maximum reflectivity over the northwestern sector of the Alps (i.e., between 6° and 11°E), characterized by regions of intense reflectivity (>30 dBZ) mixed with less intense areas (20–30 dBZ). Both the CTRL and EXP simulations capture the broader spatial pattern of the observed maximum radar reflectivity but miss some of the regions of higher values, as well as overestimate values in the 0–10-dBZ range along the southern flank of the snowfall region. Additionally, although the results from the CTRL and EXP simulations are generally similar, the observed maximum reflectivity values are slightly better represented by EXP compared to CTRL in some regions, such as over the northern sector of the Alps (10°–14°E, 48°–50°N). The second event at 1800 UTC 1 December 2023 involves northerly flow colliding with the Alps, resulting in heavy snowfall extending over its northern sector. Here, the observations show maximum radar reflectivity

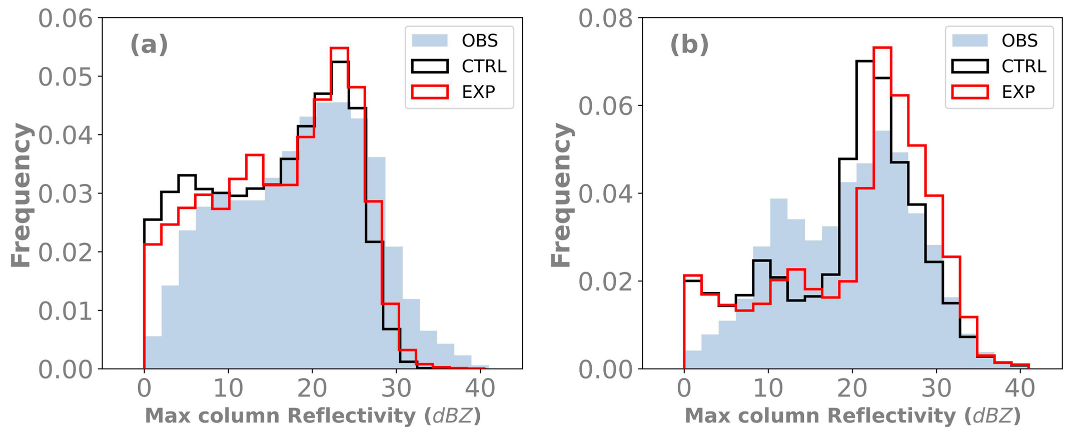

FIG. 8. Comparison of histograms of observed and modeled maximum radar reflectivity (dBZ) for the Alps at (a) 1800 UTC 12 Jan 2019 and (b) 1800 UTC 1 Dec 2023. The modeled outputs are from the CTRL and EXP simulations.

values between 20 and 30 dBZ over much of the Alps, which is broadly captured by the CTRL and EXP simulations. However, the CTRL and EXP simulations again show comparatively little differences and also show patchy regions of intense reflectivity (>30 dBZ) over the northwestern sector of the Alps that are not apparent in the observations, as well as overestimate values over the southern sector of the Alps.

Figure 8 extends this analysis by showing histograms comparing simulated and observed reflectivity for the two case studies. For the 12 January 2019 case (Fig. 8a), examination of the results shows that both simulations tend to overestimate reflectivity in the 0–8-dBZ range, which could be linked to small liquid droplets/frozen hydrometeors going undetected in observations. The results also show that model radar reflectivity values are underestimated in the 27–40-dBZ range, which is due to the model's underestimation of extreme rainfall (Fig. S5b). This limitation is illustrated in Fig. S5b, where rain reflectivity reaches up to 42 dBZ, indicative of giant raindrops, contributing significantly to the upper end of the overall reflectivity distribution. Nevertheless, both simulations reasonably capture the 8–25-dBZ range, suggesting better model performance in representing moderately intense snowfall/rainfall (Fig. 8a, Fig. S5b). Similar to the results in Fig. 7, there are only marginal differences between the CTRL and EXP simulations, although the EXP shows a slight improvement in the higher reflectivity tail of the distribution. The results for the 1 December 2023 case (Fig. 8b) are generally similar to the 12 January 2019 case, suggesting again that the simulations tend to overestimate the frequency of occurrence in the 0–8-dBZ range. However, unlike the earlier case, the model underestimates reflectivity in the 10–20-dBZ range, while better representing higher values between 25 and 40 dBZ.

It is noted that there are small but meaningful differences evident in the histograms shown in Fig. 8. In both cases, the EXP curve is shifted slightly to the right, more noticeably in Fig. 8b, which is associated with flow that has already traversed the Alps and transported moisture downwind. This suggests that residual moisture in EXP, advected farther downwind than in CTRL, may contribute to the formation of larger precipitation particles and/or new ice crystals prior to settling on the surface. Further support for this interpretation is provided in Fig. S3, which shows the spatial shift in snowfall for two distinct events over the Alps. In EXP, some downwind regions experience a net increase in snowfall, consistent with areas of high reflectivity downwind (Fig. 7f), demonstrating that model grid cells are affected differently in EXP relative to CTRL based on their positions relative to the terrain. Finally, a similar analysis was also conducted over the central Rockies using base reflectivity composites, with results similarly aligned to those over the Alps (Fig. S6).

c. *Microphysical development of snowfall extremes*

Use of a model to produce estimates of snowfall amounts also has the advantage of using its other outputs to examine the physical processes that lead to extremes, providing a better understanding of the microphysical mechanisms driven by dynamics. This includes investigation of the microphysical development of snowfall extremes and the roles played by localized forcings in the timing and intensity of precipitation. To explore this, Fig. 9 shows latitude/longitude height transects of the mixing ratios for the different hydrometeor species simulated by EXP, which are associated with extreme snowfall events occurring at Tomasee, Hampta, and Flowing Park (see Fig. 6).

The event shown for Tomasee at 1800 UTC 13 January 2019 occurs in response to the forced uplift of strong moisture-laden northwesterly winds, which elevates the lower warm layers into the subfreezing regions aloft (Fig. 9a). The vertical transects show that this uplift at first promotes ice/snow formation through heterogeneous nucleation within subfreezing layers spanning 2–8 km ASL, where temperature values extend down to −40°C. Above these layers, the cloud tops positioned between 8 and 10 km ASL exhibit even colder conditions, with temperatures below −40°C, favoring ice formation mainly via homogeneous nucleation. In the midlevel cloud region (4–8 km

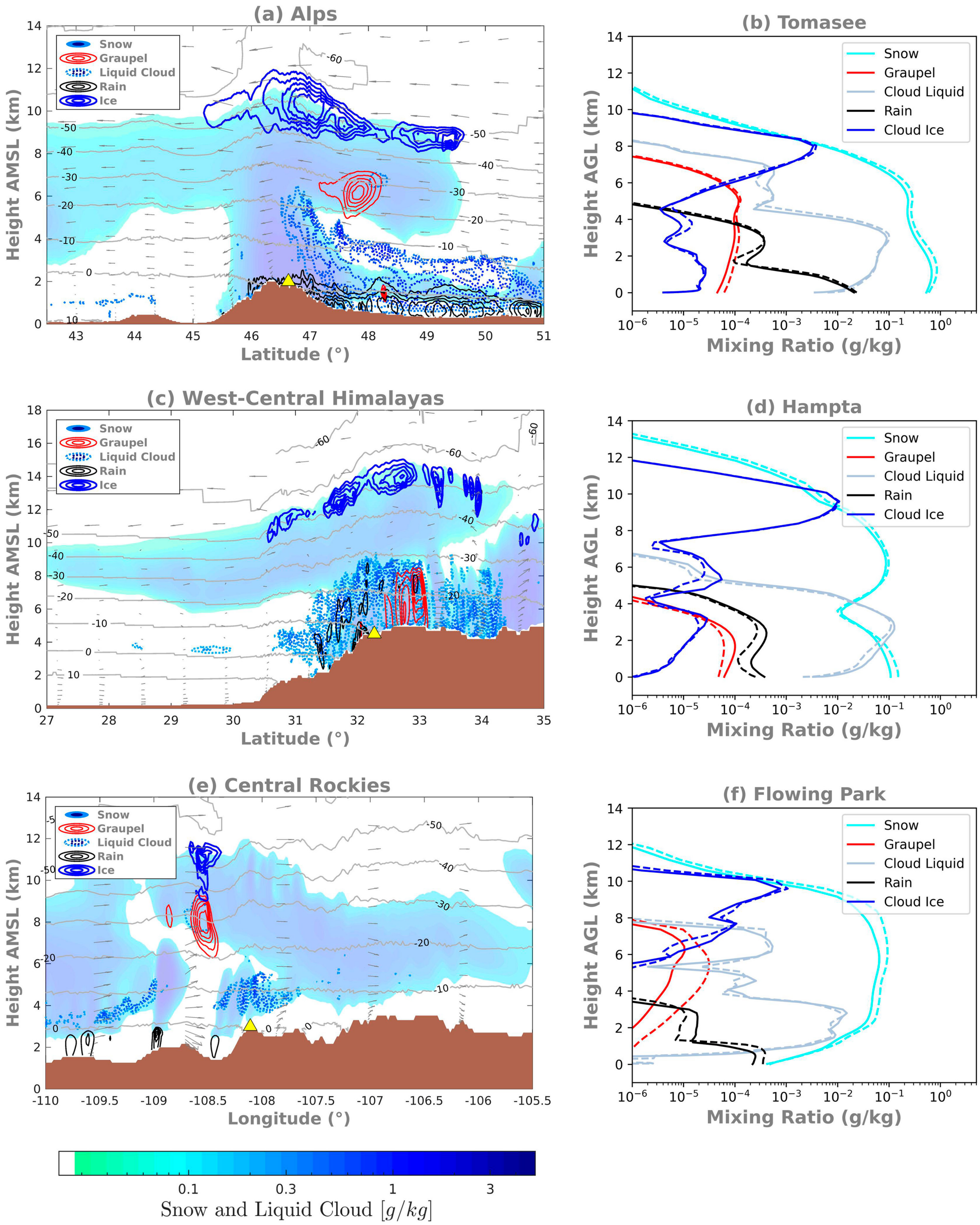

FIG. 9. Latitude–height transects of modeled hydrometeor mixing ratios (g kg^{-1}) through (a) Tomasee at 1800 UTC 13 Jan 2019 and (c) Hampta at 1800 UTC 4 Jan 2022 and (e) longitude–height transects of modeled hydrometeor mixing ratios (g kg^{-1}) through Flowing Park at 0600 UTC 2 Feb 2024. The outputs are from the EXP simulation and include snow, graupel, liquid cloud, rain, and ice hydrometeors. Note that snow (filled contours) and liquid cloud (dotted contours) have the same colormap. The brown-shaded area represents the orography, and the lake-based snowfall measurement sites are indicated by the yellow triangles. The gray lines indicate modeled temperature isotherms (°C). (b),(d),(f) Associated vertical profiles of hydrometeor mixing ratios (g kg^{-1}) from CTRL (solid lines) and EXP (dashed lines) simulations, averaged over a 1° × 1° region centered over each of the lake-based snowfall locations. Note that in (a), (c), and (e), the vertical axis is ASL, while in (b), (d), and (f), it is AGL.

ASL), the coexistence of small snow particles and supercooled liquid droplets enables the growth of these particles through droplet evaporation within the −2° to −28°C temperature range, resulting in higher snow mixing ratios. Within the same altitude band, supercooled droplets may also collide and freeze onto frozen particles, facilitating the localized production of graupel. In the bottommost 3 km ASL, which is relatively warm, both the liquid droplets and snow particles are efficiently converted to rain on the windward side of the system through a combination of cloud autoconversion and snow melting. Overall, the vertical structure reflects predominantly cold-rain processes throughout much of the atmospheric column, transitioning to warm-rain microphysics only in the lowest layers.

At Hampta, the event shown occurs at 1800 UTC 4 January 2022 in response to the orographic uplift of strong westerly winds (not shown). This shows contiguous snowbands (Fig. 9c) and a broadly similar hydrometeor distribution to the Tomasee case. However, in this case, the mixing ratios are shifted upward by approximately 2 km, reflecting the influence of high orographic elevations of the west–central Himalayas. The orographically induced stratus cloud at Hampta enhances snowfall through the seeder–feeder mechanism: Snow crystals originating from the upper-level stratus cloud (the seeder, located between 6 and 14 km ASL) act as additional nuclei for the lower mixed-phase cloud (the feeder, located between 2 and 8 km ASL). This interaction leads to increased snowfall at the surface (Gilbert et al. 2025; Fernández-González et al. 2015; Ramelli et al. 2021). It is also apparent that this event is associated with a higher preponderance of supercooled droplets positioned between the subfreezing 3 and 8 km ASL, yielding more snow as a result of droplet evaporation and vapor transport. Increased spatial coverage of liquid and snow mass within this altitude range also contributes to localized enhancements in graupel mixing ratios via riming and aggregation. The ensuing heavier and denser graupel (compared to snow) further aids the buildup of precipitation at this site. Finally, the results indicate rain activity via a combination of liquid cloud autoconverting to rain and the melting of frozen particles as they descend through the warmer atmospheric layers between 2 and 4 km ASL. Notably, rain can also be seen falling from liquid-bearing mixed-phase clouds at temperatures as cold as −27°C between 4 and 8 km ASL, suggesting that supercooled warm-rain processes could be important.

At Flowing Park, the event shown at 0600 UTC 2 February 2024 is triggered by the forced uplift of strong southerly winds (not shown). The results show an enhanced spatial extent and concentration of liquid droplets predominantly between 2 and 6 km ASL, which support increased snow production in this altitude band (Fig. 9e) and are broadly consistent with the Hampta case study. Notably, the enhanced graupel production region between 5 and 9 km ASL and around −108.5° coincides with a localized zone of elevated liquid mixing ratios, extending into colder temperatures dropping down to −36°C. This collocation likely promotes riming and aggregation processes conducive to graupel formation.

The right-hand side panels of Fig. 9 show the corresponding vertical profiles of hydrometeor mixing ratios at the same time as their latitude/longitude–height transects. In general, the figures show significant amounts of snow and ice extending to higher altitudes, also confirming with the results in the left panels. A decrease in ice mixing ratios is often accompanied by a corresponding increase in snow mixing ratios, suggesting the growth and transformation of ice crystals into snow through deposition and aggregation processes. There is a noticeable presence of supercooled liquid droplets at all the three sites, extending up to 10 km above ground level (AGL), which enhances conditions conducive to the growth of snow in the freezing layers. At Tomasee and Flowing Park (Figs. 9b,f), a sharp decline in liquid cloud water mass coincides with a runaway increase in rainwater mass in the lowest 2 km AGL, underscoring the significance of some warm rain microphysical activity in the otherwise cold cloud system. Additionally, the melting of snow and graupel may also have contributed to some rain, as indicated by the gradual downward gradients in their respective mass profiles below their peak altitudes. However, the higher elevation of these regions would limit evaporative and melt losses of the frozen hydrometeors, allowing most frozen hydrometeors to reach the surface intact.

As EXP (dashed lines) is characterized by slower-falling snow crystals, particles spend more time aloft, particularly between 3 and 7 km, resulting in higher snow mixing ratios relative to CTRL (solid lines). This has an impact on the partitioning between ice and snow, leading to a reduced vapor sink to the ice phase (e.g., over Hampta and Flowing Park) and, in some cases, slightly enhanced liquid cloud. Notably, layers with increased ice/snow and supercooled liquid water in EXP relative to CTRL—such as 3–5 km over Tomasee and 4–8 km over Flowing Park—promote riming, which in turn leads to higher graupel mixing ratios compared to CTRL. Near the surface, rain decreases slightly, likely due to reduced downward mass flux of frozen hydrometeors into warmer layers.

d. *Snowfall maps*

Finally, the ability of the high-resolution 1.5-km model to produce detailed estimates of snowfall amounts over the three target regions is examined in Fig. 10, which shows maps of the seasonal accumulated snowfall from the EXP simulation for a single winter season. Additionally, results from the relatively coarse resolution 0.25° ERA5 dataset are also included so that they can be contrasted.

The model-based snowfall maps show a large amount of heterogeneity in snowfall amounts, including pronounced localized "hot spots," reflecting the complexity of the orography in these regions. In the Alps, the total accumulated snowfall peaks along its predominantly east–west-oriented ridge, reaching values in excess of 1600 kg m^{-2}, while minimum values are mainly found over the low-lying valley floors (Fig. 10a). The results for the west–central Himalayas show snowfall values in excess of 800 kg m^{-2} along its southern slopes (above 3500 m), particularly around Manali (31°–33°N, 76°–78°E), which is nestled within the Himalayan Pir Panjal range, and surrounded by particularly sharp orography (Fig. 10c). In the central Rockies, areas of intense snowfall are more localized around high-elevation regions to the east (Fig. 10e). By contrast, the snowfall maps based on

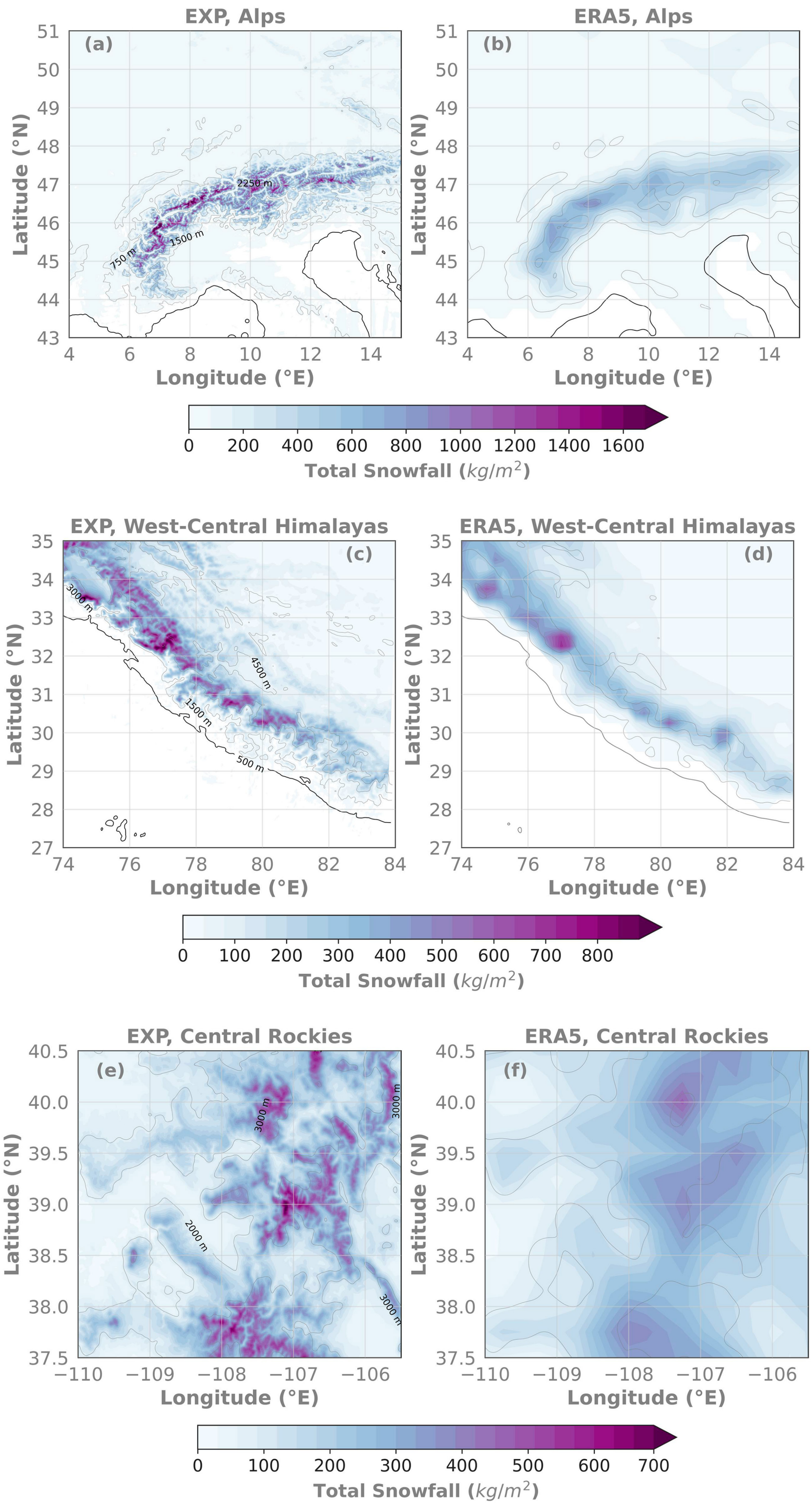

FIG. 10. Comparison of modeled and ERA5 total seasonal accumulated snowfall (kg m^{-2}) for the winter period of 2023–24 for the (a),(b) Alps and (e),(f) central Rockies and 2021–22 for the (c),(d) west–central Himalayas. The modeled outputs are from the EXP simulations. Also shown are the model orography (m; contours). Note that the snowfall for each region has a different scale.

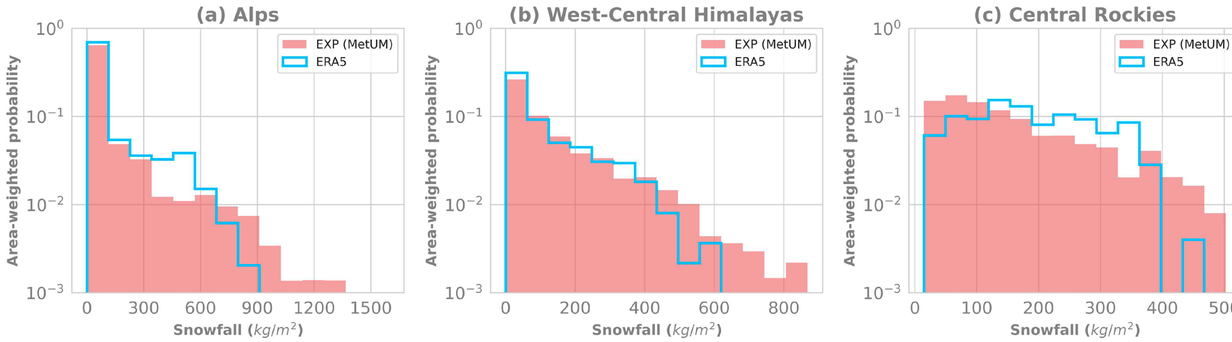

FIG. 11. Histograms of modeled and ERA5 total seasonal accumulated snowfall (kg m^{-2}) for the winter period of 2023–24 for the (a) Alps and (c) central Rockies and 2021–22 for the (b) west–central Himalayas. The modeled outputs are from the EXP simulations upscaled to the ERA5 resolution of 0.25°.

ERA5 have a much more homogenous distribution due to reduced orographic effects (Webster et al. 2008; Gilbert et al. 2025), as well as considerably reduced snowfall amounts compared to EXP, i.e., consistent with Figs. 2–6. For example, the peak value in the Alps from ERA5 is less than 1000 kg m^{-2}, which is considerably less than the EXP-based estimate of 1600 kg m^{-2} (Figs. 10a,b).

Even when EXP is upscaled to match the ERA5 resolution of 0.25°, the histograms of modeled and ERA5 total seasonal accumulated snowfall in Fig. 11 demonstrate that ERA5 fails to capture key snowfall hotspots, showing reduced amounts, particularly along the tail end of the snowfall distribution.

4. Discussion and conclusions

Comprehensive assessments of snowfall amounts in mountainous regions are currently lacking due to concerns over the sparseness and quality of snowfall measurements. These measurements are crucial for establishing baseline records and for effectively testing and constraining snowfall outputs simulated by RCMs. To address this knowledge gap, this study used unique lake-based snowfall observations in topographically complex regions in the Alps, west–central Himalayas, and central Rockies to constrain and fine tune the representation of snowfall in the kilometer-scale regional configuration of the MetUM (i.e., grid cells on a similar scale to the size of the lakes).

The results show that the simulations can reasonably capture the timing of the beginning and cessation of the snowfall events as well as measured snowfall totals, particularly for extreme events (Figs. 2–6). The overall onset bias across sites ranges between −6 and 3 h with an RMSE of 8.16 h. In terms of the snowfall amounts, EXP has an overall bias of 2.62 kg m^{-2} compared to 3.65 and −6.75 kg m^{-2} for CTRL and ERA5, respectively (Fig. S4). The good performance of the MetUM was achieved by reducing the snow terminal fall speed in the Cloud Aerosol Interaction Microphysics (CASIM) scheme to tune/adjust modeled snowfall to better match the observations. Here, the reduction in the fall speed resulted in lowering of peak snowfall amounts during extremes (Figs. 2–6), as well as redistribution of snowfall further downstream (see Fig. S3).

Results from this present work are broadly consistent with suggestions from Lim and Hong (2005), Molthan et al. (2016), and Orr et al. (2017) that simulations of precipitation extremes are sensitive to the sedimentation properties of frozen hydrometeors. Additionally, the improvement in snowfall intensities from this work conforms with the general conclusions from previous research by Maussion et al. (2011), Orr et al. (2017), and Collier and Immerzeel (2015) that RCMs tend to apportion both liquid and solid precipitation well. It is further noted that the key processes driving snowfall extremes at these high-elevation supersites are predominantly cold-rain microphysical mechanisms, transitioning to warm-rain processes only in the lowest layers (Fig. 9). Notably, seeder–feeder-type cloud interaction could be a typical mechanism for increased surface snowfall in the west–central Himalayan region (Fig. 9c), consistent with field studies from other parts of the world (Purdy et al. 2005; Hill et al. 1981).

Precipitation estimates over mountainous regions differ widely between the range of available gridded datasets (e.g., APHRODITE, TRMM, global reanalyses), which also tend to systematically underestimate extreme snowfall events (Bannister et al. 2019; Palazzi et al. 2013). As a result, there is a lack of consensus/confidence in snowfall estimates from these products in regions like High Mountain Asia/west–central Himalayas (Ji and Yuan 2020; Sun et al. 2024). In this study, the EXP simulation estimated much larger snowfall amounts compared to ERA5 (Figs. 2–6, 10, and 11), which align more closely with the observed lake-based snowfall amounts. We argue that the above uncertainty in existing gridded precipitation datasets can be overcome by considering the MetUM output as pseudo-observations and using the tuned model setup to generate long-term, high-resolution snowfall outputs that can effectively be used to increase snowfall records of extreme events in orographically complex regions that are poorly observed and understood. Moreover, machine learning and statistical models, which inherently perform best with sufficient training data, could then be trained on these model-generated records to produce quick emulation maps of snow variables in poorly observed and understood mountain locations (Girona-Mata et al. 2025).

Moreover, the outputs/pseudo-observations from the MetUM are particularly suitable for use in impact studies to assess the hydrological and socioeconomic implications of current water availability across large, mountain-fed hydroeconomies. High-resolution outputs can be used to force glacier, snowpack, and hydroeconomic models to predict future changes in water resources in each mountain region where it could be utilized for much needed improvements to hydroclimatic services (Widmann et al. 2019). In the first instance, the snowfall maps (Fig. 10) presented in this study provide valuable insights into snowfall distribution and can enhance predictions of snow-related hazards in these regions (Acharya et al. 2023). This is crucial because snowfall patterns indicate that extreme weather events play a significant role in determining seasonal snowfall totals (Figs. 2–6), a finding consistent with previous studies by Regmi and Bookhagen (2022) and Wulf et al. (2010). Therefore, an understanding of the timing of the beginning and cessation of snowfall extremes will be the key to estimating the magnitude and timing of drainage and river flows originating from these regions. This foreknowledge is essential for assessing the downstream impacts on populations that rely on mountain water resources, particularly in the face of potential water shocks.

While this study highlights a generally strong agreement between model results and observations, particularly for snowfall extremes, some potential areas for improvement are also identified. We show that although modeled reflectivity broadly agrees with the observed maximum radar reflectivity, it does not fully capture the greater variability seen in the observations (Figs. 7 and 8). However, although snowfall rate and reflectivity are physically linked, they are not directly comparable quantities, and discrepancies in reflectivity do not necessarily imply deficiencies in simulated snowfall accumulation. For example, small variations in the size and number concentration of ice or snow, produced through primary nucleation or secondary ice generation, can substantially affect reflectivity attributes (Field et al. 2023). This is particularly evident from Fig. S5b, which highlights the sensitivity of overall reflectivity to individual hydrometeor phase distributions, strongly dependent on particle size. These findings are valuable for modelers incorporating updates such as more detailed crystal specifications and improved reflectivity formulations, consistent with suggestions by Molthan et al. (2016) and Vázquez-Martín et al. (2021).

Mismatches between the observed and modeled snowfall events could also be affected by wind redistribution of snow that, along with direct precipitation, is captured by the observations but is not represented by the MetUM. Although the study lakes are large enough to be unaffected by erosion and deposition on the scale of snow drifts (unlike snow pillows, scales, pluviometers, etc.), if wind speeds are high enough and the snowpack sufficiently weakly consolidated, then locally low-lying lakes like Tomasee could tend to collect additional snow that was eroded and transported from mountain slopes at higher altitudes (Stigter et al. 2018). However, over the whole winter, the cumulative observed snowfall amount at Tomasee is slightly lower than the simulated amounts (Fig. 6b), which is the opposite sign expected if wind-driven deposition was making an important contribution here. Conversely, for locally elevated plateau/promontory lakes like Flowing Park and Hampta, they could potentially lose eroded snow to the surrounding lower ground. However, over the whole winter, the cumulative observed snowfall amounts at Flowing Park and Hampta are slightly higher than the simulated amounts (Figs. 6d,f), which is the opposite sign expected if wind-driven erosion was important for these lakes. However, to properly investigate the influence of wind-driven effects, future work could examine excluding high-wind events from model–observation comparisons. Additionally, it is also likely that model–observation mismatches could be related to the representation of convection-inducing localized diurnal mountain-valley winds, especially for low-intensity events. Adequate representation of these winds in RCMs is a long-standing issue, with several previous studies highlighting the difficulty in representing them in the Himalayas (Potter et al. 2018; Shrestha and Deshar 2015; Sato 2013; Bhatt and Nakamura 2006; Norris et al. 2017).

The relative scarcity of lake-based sites also remains a limitation, and it will therefore be beneficial to have more of such sites to better understand/validate the spatial attributes of snowfall from the MetUM. Efforts are underway to increase the density of lake-based sites, which, together with additional years of data from existing probes, should enable a more comprehensive assessment in a future study. However, despite their limited number, these measurements represent high-quality, well-calibrated observations, which makes them particularly valuable for model evaluation. For example, the total lake area sampled ($\sim$5.1 km^2; see Table 1) is on the order of 10^8 times larger than a typical point-scale pluviometer aperture ($\sim$0.03 m^2), and as such, the recorded signal effectively integrates snowfall over an area equivalent to a very large number of point-scale gauges operating simultaneously. This spatial integration reduces susceptibility to localized measurement errors and supports the use of these observations as a reliable basis for model evaluation.

To support further model assessment/improvement, future work could also perhaps focus on complementing the expanded set of lake-based observations with bias-corrected SWE estimates from gauges and snow pillows. For example, a range of bias-reduction approaches have been developed for these instruments, including design modifications, such as aerodynamically shaped gauge bodies that reduce airflow disturbance around the collection funnel and wind shields that lower wind speeds at the orifice. In addition, meteorology-based correction functions and machine learning algorithms have also been developed to improve the fidelity of SWE estimates from both gauges and snow pillows (Herbert et al. 2025; Yang et al. 2025; Cauteruccio et al. 2024; Segovia-Cardozo et al. 2023; Hongyi et al. 2023). However, the effectiveness of these approaches, in particular, the use of machine learning methods, depends heavily on the continuous availability of reliable ground truth information for benchmarking/training, which is often scarce. Furthermore, the correction procedures developed for one region are generally not transferable to other regions with different geographical and climatic settings, limiting the analyses of mountain-range scale shifts in snowfall patterns.

Finally, future work could potentially use observed aerosol fields to work out the droplet number concentrations used by the CASIM cloud microphysics scheme in the MetUM (Field et al. 2023). Deriving droplet numbers through aerosol activation impacts forecasts, especially in terms of the timing, location, and intensity of rainfall or snowfall events (Proske et al. 2024; Gumber et al. 2022; Gumber and Ghosh 2022a,b). As aerosols influence the rate at which clouds transition into precipitation—either slowing down or accelerating the process—understanding their impact could lead to more precise predictions of extreme weather events. Related to this idea would be to examine the ability of the high-resolution regional version of the MetUM with interactive aerosols (Price et al. 2025) to simulate snowfall over mountainous regions.

Acknowledgments. We dedicate this paper to the memory of Shravan Bhattaram, a promising young Ph.D student supervised by P. D. working on the microphysics of HMA snowfall at IIT Kharagpur. His untimely passing in December 2025 is a profound loss, and he will be dearly missed by his colleagues and friends. We thank the editor and two anonymous reviewers for their valuable comments and suggestions, which have greatly improved the quality of this manuscript. S. G., A. O., H. P., F. C., and P. F. were supported by the National Environmental Research Council (NERC) funded by The Big Thaw Project (NE/X005267/1). P. D. is supported by IIT Kharagpur (India) and National Geographic Society, USA (Grant NGS-61844R-19). M. G. M. is supported by U.K. Research and Innovation (Grant EP/S022961/1). This work used the ARCHER2 U.K. National Supercomputing Service. S. G., A. O., H. P., and P. F. were involved in conceptualization; S. G. and A. O. led the main writing of the manuscript; S. G., A. O., and P. F. were responsible for model data curation and methodology; F. C., H. P., and P. D. were responsible for field data collection; S. G. led the formal analysis, validation, and visualization. All authors contributed to the review and editing of the manuscript. The contact author has declared that none of the authors has any competing interests.

Data availability statement. The OPERA radar composites are available from https://portail-api.meteofrance.fr/web/en/. The Next Generation Weather Radar (NEXRAD) mosaics are available from https://mesonet.agron.iastate.edu/docs/nexrad_mosaic/. ERA5 data are available via the Copernicus Climate Data Store (https://doi.org/10.24381/cds.adbb2d47) (Hersbach et al. 2020). The snowfall amounts for the 111 events across all six lake-based sites used in this study are shown in Table S1. Model data generated or analyzed during this study are included in this published article (and its supplemental information files).

REFERENCES

Abdalla, S., L. Isaksen, P. A. E. M. Janssen, and W. Nils, 2013: Effective spectral resolution of ECMWF atmospheric forecast models 2. *ECMWF Newsletter*, No. 137, ECMWF, Reading, United Kingdom, 19–22, https://www.ecmwf.int/sites/default/files/elibrary/2013/17358-effective-spectral-resolution-ecmwf-atmospheric-forecast-models.pdf.

Acharya, A., J. F. Steiner, K. M. Walizada, S. Ali, Z. H. Zakir, A. Caiserman, and T. Watanabe, 2023: Review article: Snow and ice avalanches in high mountain Asia—scientific, local and indigenous knowledge. *Nat. Hazards Earth Syst. Sci.*, **23**, 2569–2592, https://doi.org/10.5194/nhess-23-2569-2023.

Alcott, T. I., and W. J. Steenburgh, 2013: Orographic influences on a Great Salt Lake–effect snowstorm. *Mon. Wea. Rev.*, **141**, 2432–2450, https://doi.org/10.1175/MWR-D-12-00328.1.

An, W., S. Hou, Y. Hu, and S. Wu, 2017: Delayed warming hiatus over the Tibetan Plateau. *Earth Space Sci.*, **4**, 128–137, https://doi.org/10.1002/2016EA000179.

Andermann, C., S. Bonnet, and R. Gloaguen, 2011: Evaluation of precipitation data sets along the Himalayan front. *Geochem. Geophys. Geosyst.*, **12**, Q07023, https://doi.org/10.1029/2011GC003513.

Archer, D. R., and H. J. Fowler, 2004: Spatial and temporal variations in precipitation in the Upper Indus Basin, global teleconnections and hydrological implications. *Hydrol. Earth Syst. Sci.*, **8**, 47–61, https://doi.org/10.5194/hess-8-47-2004.

Bannister, D., and Coauthors, 2019: Bias correction of high-resolution regional climate model precipitation output gives the best estimates of precipitation in Himalayan catchments. *J. Geophys. Res. Atmos.*, **124**, 14 220–14 239, https://doi.org/10.1029/2019JD030804.

Barnett, T. P., J. C. Adam, and D. P. Lettenmaier, 2005: Potential impacts of a warming climate on water availability in snow-dominated regions. *Nature*, **438**, 303–309, https://doi.org/10.1038/nature04141.

Baudouin, J.-P., M. Herzog, and C. A. Petrie, 2020: Contribution of cross-barrier moisture transport to precipitation in the upper Indus River basin. *Mon. Wea. Rev.*, **148**, 2801–2818, https://doi.org/10.1175/MWR-D-19-0384.1.

Beck, H. E., E. F. Wood, T. R. McVicar, M. Zambrano-Bigiarini, C. Alvarez-Garreton, O. M. Baez-Villanueva, J. Sheffield, and D. N. Karger, 2020: Bias correction of global high-resolution precipitation climatologies using streamflow observations from 9372 catchments. *J. Climate*, **33**, 1299–1315, https://doi.org/10.1175/JCLI-D-19-0332.1.

Bharati, P., P. Deb, K. M. R. Hunt, A. Orr, and M. K. Dash, 2025: ENSO-induced latitudinal variation of the subtropical jet modulates extreme winter precipitation over the western Himalaya. *Adv. Atmos. Sci.*, **42**, 427–437, https://doi.org/10.1007/s00376-024-4057-2.

Bhatt, B. C., and K. Nakamura, 2006: A climatological-dynamical analysis associated with precipitation around the southern part of the Himalayas. *J. Geophys. Res.*, **111**, D02115, https://doi.org/10.1029/2005JD006197.

Bookhagen, B., and D. W. Burbank, 2010: Toward a complete Himalayan hydrological budget: Spatiotemporal distribution of snowmelt and rainfall and their impact on river discharge. *J. Geophys. Res.*, **115**, F03019, https://doi.org/10.1029/2009JF001426.

Boutle, I. A., J. E. J. Eyre, and A. P. Lock, 2014: Seamless stratocumulus simulation across the turbulent gray zone. *Mon. Wea. Rev.*, **142**, 1655–1668, https://doi.org/10.1175/MWR-D-13-00229.1.

Bush, M., and Coauthors, 2025: The third Met Office Unified Model–JULES Regional Atmosphere and Land Configuration, RAL3. *Geosci. Model Dev.*, **18**, 3819–3855, https://doi.org/10.5194/gmd-18-3819-2025.

Cauteruccio, A., E. Chinchella, and L. G. Lanza, 2024: The overall collection efficiency of catching-type precipitation gauges in windy conditions. *Water Resour. Res.*, **60**, e2023WR035098, https://doi.org/10.1029/2023WR035098.

Chandra, A., S. Ghosh, N. Doshi, S. Deshpande, and S. Gumber, 2020: A case study on assessing cumulonimbus induced flight vulnerabilities over the Nepalese Himalayan terrain. *Pure Appl.*

Geophys., **177**, 5041–5066, https://doi.org/10.1007/s00024-020-02541-w.

Colle, B. A., and Y. Zeng, 2004: Bulk microphysical sensitivities within the MM5 for orographic precipitation. Part I: The Sierra 1986 event. *Mon. Wea. Rev.*, **132**, 2780–2801, https://doi.org/10.1175/MWR2821.1.

Collier, E., and W. W. Immerzeel, 2015: High-resolution modeling of atmospheric dynamics in the Nepalese Himalaya. *J. Geophys. Res. Atmos.*, **120**, 9882–9896, https://doi.org/10.1002/2015JD023266.

Currier, W. R., T. Thorsona, and J. D. Lundquist, 2017: Independent evaluation of frozen precipitation from WRF and PRISM in the Olympic Mountains. *J. Hydrometeor.*, **18**, 2681–2703, https://doi.org/10.1175/JHM-D-17-0026.1.

Derin, Y., and Coauthors, 2016: Multiregional satellite precipitation products evaluation over complex terrain. *J. Hydrometeor.*, **17**, 1817–1836, https://doi.org/10.1175/JHM-D-15-0197.1.

Dimri, A. P., D. Niyogi, A. P. Barros, J. Ridley, U. C. Mohanty, T. Yasunari, and D. R. Sikka, 2015: Western disturbances: A review. *Rev. Geophys.*, **53**, 225–246, https://doi.org/10.1002/2014RG000460.

Durand, Y., G. Giraud, M. Laternser, P. Etchevers, L. Mérindol, and B. Lesaffre, 2009: Reanalysis of 47 years of climate in the French Alps (1958–2005): Climatology and trends for snow cover. *J. Appl. Meteor. Climatol.*, **48**, 2487–2512, https://doi.org/10.1175/2009JAMC1810.1.

ECMWF, 2021: IFS documentation CY47R3–Part I: Observations. IFS Doc. CY47R3, 82 pp., https://www.ecmwf.int/en/elibrary/81268-ifs-documentation-cy47r3-part-i-observations.

Edwards, J. M., and A. Slingo, 1996: Studies with a flexible new radiation code. I: Choosing a configuration for a large-scale model. *Quart. J. Roy. Meteor. Soc.*, **122**, 689–719, https://doi.org/10.1002/qj.49712253107.

Farr, T. G., and Coauthors, 2007: The Shuttle Radar Topography Mission. *Rev. Geophys.*, **45**, RG2004, https://doi.org/10.1029/2005RG000183.

Fernández-González, S., F. Valero, J. L. Sánchez, E. Gascón, L. López, E. García-Ortega, and A. Merino, 2015: Analysis of a seeder-feeder and freezing drizzle event. *J. Geophys. Res. Atmos.*, **120**, 3984–3999, https://doi.org/10.1002/2014JD022916.

Field, P. R., and Coauthors, 2023: Implementation of a double moment cloud microphysics scheme in the UK Met Office regional numerical weather prediction model. *Quart. J. Roy. Meteor. Soc.*, **149**, 703–739, https://doi.org/10.1002/qj.4414.

Garrett, T. J., C. Fallgatter, K. Shkurko, and D. Howlett, 2012: Fall speed measurement and high-resolution multi-angle photography of hydrometeors in free fall. *Atmos. Meas. Tech.*, **5**, 2625–2633, https://doi.org/10.5194/amt-5-2625-2012.

Garvert, M. F., B. A. Colle, and C. F. Mass, 2005: The 13–14 December 2001 IMPROVE-2 event. Part I: Synoptic and mesoscale evolution and comparison with a mesoscale model simulation. *J. Atmos. Sci.*, **62**, 3474–3492, https://doi.org/10.1175/JAS3549.1.

Ghosh, S., D. K. Barik, P. Renganayaki, B. Kang, S. Gumber, S. Venkatesh, D. S. Saini, and S. Akunuri, 2023: The impact of short-duration precipitation events over the historic Cauvery basin: A study on altered water resource patterns and associated threats. *Sci. Rep.*, **13**, 14095, https://doi.org/10.1038/s41598-023-41417-6.

Gilbert, E., D. Pishniak, J. A. Torres, A. Orr, M. Maclennan, N. Wever, and K. Verro, 2025: Extreme precipitation associated with atmospheric rivers over West Antarctic ice shelves: Insights from kilometre-scale regional climate modelling. *Cryosphere*, **19**, 597–618, https://doi.org/10.5194/tc-19-597-2025.

Girona-Mata, M., and Coauthors, 2025: Probabilistic precipitation downscaling for ungauged mountain sites: A pilot study for the Hindu Kush Himalaya. *Hydrol. Earth Syst. Sci.*, **29**, 3073–3100, https://doi.org/10.5194/hess-29-3073-2025.

Goodison, B. E., P. Y. T. Louie, and D. Yang, 1998: WMO Solid precipitation measurement intercomparison–final report | enhanced reader. Instruments and Observing Methods Rep. 67, WMO/TD-872, 212 pp., https://library.wmo.int/records/item/28336-wmo-solid-precipitation-measurement-intercomparison.

Gumber, S., and S. Ghosh, 2022a: An experimental and modelling analysis of cloud droplet growth from vehicular emissions with non-ideal microphysics over an Asian mega-city. *Atmos. Sci. Lett.*, **23**, e1081, https://doi.org/10.1002/asl.1081.

——, and ——, 2022b: Quick predictions of onset times and rain amounts from monsoon showers over urban built environments. *Atmosphere*, **13**, 370, https://doi.org/10.3390/atmos13030370.

——, ——, S. Bera, and T. V. Prabhakaran, 2022: On the importance of non-ideal sulphate processing of multi-component aerosol haze over urban areas. *Meteor. Atmos. Phys.*, **134**, 37, https://doi.org/10.1007/s00703-022-00877-7.

——, S. Bera, S. Ghosh, and T. V. Prabhakaran, 2024: Turbulence-induced droplet grouping and augmented rain formation in cumulus clouds. *Sci. Rep.*, **14**, 10298, https://doi.org/10.1038/s41598-024-61036-z.

Gutmann, E. D., R. M. Rasmussen, C. Liu, K. Ikeda, D. J. Gochis, M. P. Clark, J. Dudhia, and G. Thompson, 2012: A comparison of statistical and dynamical downscaling of winter precipitation over complex terrain. *J. Climate*, **25**, 262–281, https://doi.org/10.1175/2011JCLI4109.1.

Henn, B., M. P. Clark, D. Kavetski, A. J. Newman, M. Hughes, B. McGurk, and J. D. Lundquist, 2018: Spatiotemporal patterns of precipitation inferred from streamflow observations across the Sierra Nevada mountain range. *J. Hydrol.*, **556**, 993–1012, https://doi.org/10.1016/j.jhydrol.2016.08.009.

Herbert, J. N., M. S. Raleigh, and E. E. Small, 2025: Using a random forest model to combine airborne lidar and Snotel data for daily estimates of snow depth across mountain drainage basins of Colorado. *Water Resour. Res.*, **61**, e2024WR039775, https://doi.org/10.1029/2024WR039775.

Hersbach, H., and Coauthors, 2020: The ERA5 global reanalysis. *Quart. J. Roy. Meteor. Soc.*, **146**, 1999–2049, https://doi.org/10.1002/qj.3803.

Heymsfield, A., A. Bansemer, G. Heymsfield, D. Noone, M. Grecu, and D. Toohey, 2023: Relationship of multiwavelength radar measurements to ice microphysics from the IMPACTS field program. *J. Appl. Meteor. Climatol.*, **62**, 289–315, https://doi.org/10.1175/JAMC-D-22-0057.1.

Hiemstra, C. A., G. E. Liston, and W. A. Reiners, 2006: Observing, modelling, and validating snow redistribution by wind in a Wyoming upper treeline landscape. *Ecol. Modell.*, **197**, 35–51, https://doi.org/10.1016/j.ecolmodel.2006.03.005.

Hill, F. F., K. A. Browning, and M. J. Bader, 1981: Radar and raingauge observations of orographic rain over south Wales. *Quart. J. Roy. Meteor. Soc.*, **107**, 643–670, https://doi.org/10.1002/qj.49710745312.

Hock, R., and Coauthors, 2019: High mountain areas. *Ocean and Cryosphere in a Changing Climate*, H.-O. Pörtner et al., Eds., Cambridge University Press, 131–202.

Hongyi, L., Y. Zhang, H. Lei, and X. Hao, 2023: Machine learning-based bias correction of precipitation measurements at high altitude. *Remote Sens.*, **15**, 2180, https://doi.org/10.3390/rs15082180.

Honnert, R., V. Masson, C. Lac, and T. Nagel, 2021: A theoretical analysis of mixing length for atmospheric models from micro to large scales. *Front. Earth Sci.*, **8**, 582056, https://doi.org/10.3389/feart.2020.582056.

Houze, R. A., Jr., 2012: Orographic effects on precipitating clouds. *Rev. Geophys.*, **50**, RG1001, https://doi.org/10.1029/2011RG000365.

Huffman, G. J., and Coauthors, 2007: The TRMM Multisatellite Precipitation Analysis (TMPA): Quasi-global, multiyear, combined-sensor precipitation estimates at fine scales. *J. Hydrometeor.*, **8**, 38–55, https://doi.org/10.1175/JHM560.1.

Hunt, K. M. R., and Coauthors, 2025: Western disturbances and climate variability: A review of recent developments. *Wea. Climate Dyn.*, **6**, 43–112, https://doi.org/10.5194/wcd-6-43-2025.

Immerzeel, W. W., L. P. H. Van Beek, and M. F. P. Bierkens, 2010: Climate change will affect the Asian water towers. *Science*, **328**, 1382–1385, https://doi.org/10.1126/science.1183188.

——, N. Wanders, A. F. Lutz, J. M. Shea, and M. F. P. Bierkens, 2015: Reconciling high-altitude precipitation in the upper Indus basin with glacier mass balances and runoff. *Hydrol. Earth Syst. Sci.*, **19**, 4673–4687, https://doi.org/10.5194/hess-19-4673-2015.

——, and Coauthors, 2020: Importance and vulnerability of the world's water towers. *Nature*, **577**, 364–369, https://doi.org/10.1038/s41586-019-1822-y.

Isotta, F. A., and Coauthors, 2014: The climate of daily precipitation in the Alps: Development and analysis of a high-resolution grid dataset from pan-Alpine rain-gauge data. *Int. J. Climatol.*, **34**, 1657–1675, https://doi.org/10.1002/joc.3794.

Jensen, A. A., P. T. Bergmaier, B. Geerts, H. Morrison, and L. S. Campbell, 2020: Sensitivity of convective cell dynamics and microphysics to model resolution for the OWLeS IOP2b lake-effect snowband. *Mon. Wea. Rev.*, **148**, 3305–3328, https://doi.org/10.1175/MWR-D-19-0320.1.

Ji, P., and X. Yuan, 2020: Underestimation of the warming trend over the Tibetan Plateau during 1998–2013 by global land data assimilation systems and atmospheric reanalyses. *J. Meteor. Res.*, **34**, 88–100, https://doi.org/10.1007/s13351-020-9100-3.

Kajikawa, M., 1973: Laboratory measurement of falling velocity of individual ice crystals. *J. Meteor. Soc. Japan*, **51**, 263–272, https://doi.org/10.2151/jmsj1965.51.4_263.

Karki, R., S. Ul Hasson, U. Schickhoff, T. Scholten, and J. Böhner, 2017: Rising precipitation extremes across Nepal. *Climate*, **5**, 4, https://doi.org/10.3390/cli5010004.

Khanal, S., S. Tiwari, A. F. Lutz, B. V. D. Hurk, and W. W. Immerzeel, 2023: Historical climate trends over High Mountain Asia derived from ERA5 reanalysis data. *J Appl. Meteor. Climatol.*, **62**, 263–288, https://doi.org/10.1175/JAMC-D-21-0045.1.

Khvorostyanov, V. I., and J. A. Curry, 2002: Terminal velocities of droplets and crystals: Power laws with continuous parameters over the size spectrum. *J. Atmos. Sci.*, **59**, 1872–1884, https://doi.org/10.1175/1520-0469(2002)059<1872:TVODAC>2.0.CO;2.

Kou, L., Z. Lin, H. Gao, S. Liao, and P. Ding, 2023: Simulation and sensitivity analysis for cloud and precipitation measurements via spaceborne millimeter-wave radar. *Atmos. Meas. Tech.*, **16**, 1723–1744, https://doi.org/10.5194/amt-16-1723-2023.

Krishnan, R., and Coauthors, 2019: Unravelling climate change in the Hindu Kush Himalaya: Rapid warming in the mountains and increasing extremes. *The Hindu Kush Himalaya Assessment: Mountains, Climate Change, Sustainability and People*, P. Wester et al., Eds., 57–97, Springer, https://doi.org/10.1007/978-3-319-92288-1_3.

Kuhn, T., and I. Gultepe, 2016: Ice fog and light snow measurements using a high-resolution camera system. *Pure Appl. Geophys.*, **173**, 3049–3064, https://doi.org/10.1007/s00024-016-1343-7.

Lim, J.-O. J., and S.-Y. Hong, 2005: Effects of bulk ice microphysics on the simulated monsoonal precipitation over east Asia. *J. Geophys. Res.*, **110**, D24201, https://doi.org/10.1029/2005JD006166.

Lin, Y.-L., R. D. Farley, and H. D. Orville, 1983: Bulk parameterization of the snow field in a cloud model. *J. Climate Appl. Meteor.*, **22**, 1065–1092, https://doi.org/10.1175/1520-0450(1983)022<1065:BPOTSF>2.0.CO;2.

Listowski, C., and T. Lachlan-Cope, 2017: The microphysics of clouds over the Antarctic Peninsula—Part 2: Modelling aspects within Polar WRF. *Atmos. Chem. Phys.*, **17**, 10 195–10 221, https://doi.org/10.5194/acp-17-10195-2017.

Lock, A. P., A. R. Brown, M. R. Bush, G. M. Martin, and R. N. B. Smith, 2000: A new boundary layer mixing scheme. Part I: Scheme description and single-column model tests. *Mon. Wea. Rev.*, **128**, 3187–3199, https://doi.org/10.1175/1520-0493(2000)128<3187:ANBLMS>2.0.CO;2.

Madhura, R. K., R. Krishnan, J. V. Revadekar, M. Mujumdar, and B. N. Goswami, 2015: Changes in western disturbances over the Western Himalayas in a warming environment. *Climate Dyn.*, **44**, 1157–1168, https://doi.org/10.1007/s00382-014-2166-9.

Maussion, F., D. Scherer, R. Finkelnburg, J. Richters, W. Yang, and T. Yao, 2011: WRF simulation of a precipitation event over the Tibetan Plateau, China—An assessment using remote sensing and ground observations. *Hydrol. Earth Syst. Sci.*, **15**, 1795–1817, https://doi.org/10.5194/hess-15-1795-2011.

Ménégoz, M., H. Gallée, and H. W. Jacobi, 2013: Precipitation and snow cover in the Himalaya: From reanalysis to regional climate simulations. *Hydrol. Earth Syst. Sci.*, **17**, 3921–3936, https://doi.org/10.5194/hess-17-3921-2013.

Menne, M. J., I. Durre, R. S. Vose, B. E. Gleason, and T. G. Houston, 2012: An overview of the Global Historical Climatology Network-Daily database. *J. Atmos. Oceanic Technol.*, **29**, 897–910, https://doi.org/10.1175/JTECH-D-11-00103.1.

Milbrandt, J. A., and M. K. Yau, 2005: A multimoment bulk microphysics parameterization. Part II: A proposed three-moment closure and scheme description. *J. Atmos. Sci.*, **62**, 3065–3081, https://doi.org/10.1175/JAS3535.1.

Milly, P. C. D., and K. A. Dunne, 2002: Macroscale water fluxes 1. Quantifying errors in the estimation of basin mean precipitation. *Water Resour. Res.*, **38**, 1205, https://doi.org/10.1029/2001WR000759.

Miltenberger, A. K., P. R. Field, A. A. Hill, P. Rosenberg, B. J. Shipway, J. M. Wilkinson, R. Scovell, and A. M. Blyth, 2018: Aerosol–cloud interactions in mixed-phase convective clouds—Part 1: Aerosol perturbations. *Atmos. Chem. Phys.*, **18**, 3119–3145, https://doi.org/10.5194/acp-18-3119-2018.

Mishra, B., S. Panthi, B. R. Ghimire, S. Poudel, B. Maharjan, and Y. Mishra, 2023: Gridded precipitation products on the Hindu Kush-Himalaya: Performance and accuracy of seven precipitation products. *PLOS Water*, **2**, e0000145, https://doi.org/10.1371/journal.pwat.0000145.

Molthan, A. L., B. A. Colle, S. E. Yuter, and D. Stark, 2016: Comparisons of modeled and observed reflectivities and fall speeds for snowfall of varied riming degrees during winter storms on Long Island, New York. *Mon. Wea. Rev.*, **144**, 4327–4347, https://doi.org/10.1175/mwr-d-15-0397.1.

Monteiro, D., and S. Morin, 2023: Multi-decadal analysis of past winter temperature, precipitation and snow cover data in the European Alps from reanalyses, climate models and observational datasets. *Cryosphere*, **17**, 3617–3660, https://doi.org/10.5194/tc-17-3617-2023.

Morrison, H., and J. A. Milbrandt, 2015: Parameterization of cloud microphysics based on the prediction of bulk ice particle properties. Part I: Scheme description and idealized tests. *J. Atmos. Sci.*, **72**, 287–311, https://doi.org/10.1175/JAS-D-14-0065.1.

——, G. Thompson, and V. Tatarskii, 2009: Impact of cloud microphysics on the development of trailing stratiform precipitation in a simulated squall line: Comparison of one- and two-moment schemes. *Mon. Wea. Rev.*, **137**, 991–1007, https://doi.org/10.1175/2008MWR2556.1.

Norris, J., L. M. V. Carvalho, C. Jones, F. Cannon, B. Bookhagen, E. Palazzi, and A. A. Tahir, 2017: The spatiotemporal variability of precipitation over the Himalaya: Evaluation of one-year WRF model simulation. *Climate Dyn.*, **49**, 2179–2204, https://doi.org/10.1007/s00382-016-3414-y.

——, ——, ——, and ——, 2020: Warming and drying over the central Himalaya caused by an amplification of local mountain circulation. *npj Climate Atmos. Sci.*, **3**, 1, https://doi.org/10.1038/s41612-019-0105-5.

Ohara, N., M. L. Kavvas, S. Kure, Z. Q. Chen, S. Jang, and E. Tan, 2011: Physically based estimation of maximum precipitation over American River watershed, California. *J. Hydrol. Eng.*, **16**, 351–361, https://doi.org/10.1061/(ASCE)HE.1943-5584.0000324.

Orr, A., C. Listowski, M. Couttet, E. Collier, W. Immerzeel, P. Deb, and D. Bannister, 2017: Sensitivity of simulated summer monsoonal precipitation in Langtang Valley, Himalaya, to cloud microphysics schemes in WRF. *J. Geophys. Res. Atmos.*, **122**, 6298–6318, https://doi.org/10.1002/2016JD025801.

——, and Coauthors, 2022: Knowledge priorities on climate change and water in the Upper Indus Basin: A horizon scanning exercise to identify the top 100 research questions in social and natural sciences. *Earth's Future*, **10**, e2021EF002619, https://doi.org/10.1029/2021EF002619.

——, and Coauthors, 2023: Characteristics of surface "melt potential" over Antarctic ice shelves based on regional atmospheric model simulations of summer air temperature extremes from 1979/80 to 2018/19. *J. Climate*, **36**, 3357–3383, https://doi.org/10.1175/JCLI-D-22-0386.1.

Ortner, G., M. Bründl, C. M. Kropf, T. Röösli, Y. Bühler, and D. N. Bresch, 2023: Large-scale risk assessment on snow avalanche hazard in alpine regions. *Nat. Hazards Earth Syst. Sci.*, **23**, 2089–2110, https://doi.org/10.5194/nhess-23-2089-2023.

Palazzi, E., J. Von Hardenberg, and A. Provenzale, 2013: Precipitation in the Hindu-Kush Karakoram Himalaya: Observations and future scenarios. *J. Geophys. Res. Atmos.*, **118**, 85–100, https://doi.org/10.1029/2012JD018697.

Pflug, J. M., S. A. Margulis, and J. D. Lundquist, 2022: Inferring watershed-scale mean snowfall magnitude and distribution using multidecadal snow reanalysis patterns and snow pillow observations. *Hydrol. Processes*, **36**, e14581, https://doi.org/10.1002/hyp.14581.

Pörtner, H. O., and Coauthors, 2022: *The Ocean and Cryosphere in a Changing Climate.* Cambridge University Press, 756 pp., https://doi.org/10.1017/9781009157964.

Potter, E. R., A. Orr, I. C. Willis, D. Bannister, and F. Salerno, 2018: Dynamical drivers of the local wind regime in a Himalayan valley. *J. Geophys. Res. Atmos.*, **123**, 13 186–13 202, https://doi.org/10.1029/2018JD029427.

——, and Coauthors, 2023: A future of extreme precipitation and droughts in the Peruvian Andes. *npj Climate Atmos. Sci.*, **6**, 96, https://doi.org/10.1038/s41612-023-00409-z.

Price, R., A. Orr, P. F. Field, G. Mace, and A. Protat, 2025: Simulation of cloud processes over offshore coastal Antarctica using the high-resolution regional UK Met Office Unified Model with interactive aerosols. *J. Geophys. Res. Atmos.*, **130**, e2024JD042109, https://doi.org/10.1029/2024JD042109.

Pritchard, H. D., 2019: Asia's shrinking glaciers protect large populations from drought stress. *Nature*, **569**, 649–654, https://doi.org/10.1038/s41586-019-1240-1.

——, 2021: Global data gaps in our knowledge of the terrestrial cryosphere. *Front. Climate*, **3**, 689823, https://doi.org/10.3389/fclim.2021.689823.

——, D. Farinotti, and S. Colwell, 2021: Measuring changes in snowpack SWE continuously on a landscape scale using lake water pressure. *J. Hydrometeor.*, **22**, 795–811, https://doi.org/10.1175/JHM-D-20-0206.1.

Proske, U., S. Ferrachat, and U. Lohmann, 2024: Developing a climatological simplification of aerosols to enter the cloud microphysics of a global climate model. *Atmos. Chem. Phys.*, **24**, 5907–5933, https://doi.org/10.5194/acp-24-5907-2024.

Purdy, J. C., G. L. Austin, A. W. Seed, and I. D. Cluckie, 2005: Radar evidence of orographic enhancement due to the seeder feeder mechanism. *Meteor. Appl.*, **12**, 199–206, https://doi.org/10.1017/S1350482705001672.

Ramelli, F., and Coauthors, 2021: Microphysical investigation of the seeder and feeder region of an Alpine mixed-phase cloud. *Atmos. Chem. Phys.*, **21**, 6681–6706, https://doi.org/10.5194/acp-21-6681-2021.

Rasmussen, R., and Coauthors, 2012: How well are we measuring snow: The NOAA/FAA/NCAR winter precipitation test bed. *Bull. Amer. Meteor. Soc.*, **93**, 811–829, https://doi.org/10.1175/BAMS-D-11-00052.1.

Regmi, S., and B. Bookhagen, 2022: The spatial pattern of extreme precipitation from 40 years of gauge data in the central Himalaya. *Wea. Climate Extremes*, **37**, 100470, https://doi.org/10.1016/j.wace.2022.100470.

Roe, G. H., 2005: Orographic precipitation. *Annu. Rev. Earth Planet. Sci.*, **33**, 645–671, https://doi.org/10.1146/annurev.earth.33.092203.122541.

Sabin, T. P., R. Krishnan, R. Vellore, P. Priya, H. P. Borgaonkar, B. B. Singh, and A. Sagar, 2020: Climate change over the Himalayas. *Assessment of Climate Change over the Indian Region*, R. Krishnan et al., Eds., Springer, 207–222, https://doi.org/10.1007/978-981-15-4327-2_11.

Saltikoff, E., and Coauthors, 2019: OPERA the radar project. *Atmosphere*, **10**, 320, https://doi.org/10.3390/atmos10060320.

Sato, T., 2013: Mechanism of orographic precipitation around the Meghalaya Plateau associated with intraseasonal oscillation and the diurnal cycle. *Mon. Wea. Rev.*, **141**, 2451–2466, https://doi.org/10.1175/MWR-D-12-00321.1.

Schoenberg Ferrier, B., 1994: A double-moment multiple-phase four-class bulk ice scheme. Part I: Description. *J. Atmos. Sci.*, **51**, 249–280, https://doi.org/10.1175/1520-0469(1994)051<0249:ADMMPF>2.0.CO;2.

Segovia-Cardozo, D. A., C. Bernal-Basurco, and L. Rodríguez-Sinobas, 2023: Tipping bucket rain gauges in hydrological research: Summary on measurement uncertainties, calibration, and error reduction strategies. *Sensors*, **23**, 5385, https://doi.org/10.3390/s23125385.

Shannon, S., A. Payne, J. Freer, G. Coxon, M. Kauzlaric, D. Kriegel, and S. Harrison, 2023: A snow and glacier hydrological model for large catchments—Case study for the Naryn River, central Asia. *Hydrol. Earth Syst. Sci.*, **27**, 453–480, https://doi.org/10.5194/hess-27-453-2023.

Shrestha, D., and R. Deshar, 2015: Spatial variations in the diurnal pattern of precipitation over Nepal Himalayas. *Nepal J. Sci. Technol.*, **15**, 57–64, https://doi.org/10.3126/njst.v15i2.12116.

Sterzinger, L. J., and A. L. Igel, 2021: The effects of ice habit on simulated orographic snowfall. *J. Hydrometeor.*, **22**, 1649–1661, https://doi.org/10.1175/JHM-D-20-0253.1.

Stigter, E. E., M. Litt, J. F. Steiner, P. N. J. Bonekamp, J. M. Shea, M. F. P. Bierkens, and W. W. Immerzeel, 2018: The importance of snow sublimation on a Himalayan glacier. *Front. Earth Sci.*, **6**, 108, https://doi.org/10.3389/feart.2018.00108.

Sun, F., and Coauthors, 2024: Decreasing trends of mean and extreme snowfall in High Mountain Asia. *Sci. Total Environ.*, **921**, 171211, https://doi.org/10.1016/j.scitotenv.2024.171211.

Takasuka, D., and Coauthors, 2024: How can we improve the seamless representation of climatological statistics and weather toward reliable global k-scale climate simulations? *J. Adv. Model. Earth Syst.*, **16**, e2023MS003701, https://doi.org/10.1029/2023MS003701.

Tarek, M., F. P. Brissette, and R. Arsenault, 2020: Evaluation of the ERA5 reanalysis as a potential reference dataset for hydrological modelling over North America. *Hydrol. Earth Syst. Sci.*, **24**, 2527–2544, https://doi.org/10.5194/hess-24-2527-2020.

Taszarek, M., J. T. Allen, M. Marchio, and H. E. Brooks, 2021: Global climatology and trends in convective environments from ERA5 and rawinsonde data. *npj Climate Atmos. Sci.*, **4**, 35, https://doi.org/10.1038/s41612-021-00190-x.

Thompson, G., P. R. Field, R. M. Rasmussen, and W. D. Hall, 2008: Explicit forecasts of winter precipitation using an improved bulk microphysics scheme. Part II: Implementation of a new snow parameterization. *Mon. Wea. Rev.*, **136**, 5095–5115, https://doi.org/10.1175/2008MWR2387.1.

Tobin, C., A. Rinaldo, and B. Schaefli, 2012: Snowfall limit forecasts and hydrological modeling. *J. Hydrometeor.*, **13**, 1507–1519, https://doi.org/10.1175/JHM-D-11-0147.1.

Van Weverberg, K., C. J. Morcrette, I. Boutle, K. Furtado, and P. R. Field, 2021: A bimodal diagnostic cloud fraction parameterization. Part I: Motivating analysis and scheme description. *Mon. Wea. Rev.*, **149**, 841–857, https://doi.org/10.1175/MWR-D-20-0224.1.

Vázquez-Martín, S., T. Kuhn, and S. Eliasson, 2021: Mass of different snow crystal shapes derived from fall speed measurements. *Atmos. Chem. Phys.*, **21**, 18 669–18 688, https://doi.org/10.5194/acp-21-18669-2021.

Viviroli, D., and Coauthors, 2011: Climate change and mountain water resources: Overview and recommendations for research, management and policy. *Hydrol. Earth Syst. Sci.*, **15**, 471–504, https://doi.org/10.5194/hess-15-471-2011.

Walters, D., and Coauthors, 2019: The Met Office Unified Model Global Atmosphere 7.0/7.1 and JULES Global Land 7.0 configurations. *Geosci. Model Dev.*, **12**, 1909–1963, https://doi.org/10.5194/gmd-12-1909-2019.

Wang, X., V. Tolksdorf, M. Otto, and D. Scherer, 2021: WRF-based dynamical downscaling of ERA5 reanalysis data for High Mountain Asia: Towards a new version of the High Asia Refined analysis. *Int. J. Climatol.*, **41**, 743–762, https://doi.org/10.1002/joc.6686.

Webster, S., M. Uddstrom, H. Oliver, and S. Vosper, 2008: A high-resolution modelling case study of a severe weather event over New Zealand. *Atmos. Sci. Lett.*, **9**, 119–128, https://doi.org/10.1002/asl.172.

Westbrook, C. D., R. C. Ball, and P. R. Field, 2006: Radar scattering by aggregate snowflakes. *Quart. J. Roy. Meteor. Soc.*, **132**, 897–914, https://doi.org/10.1256/qj.05.82.

Wester, P., A. Mishra, A. Mukherji, and A. B. Shrestha, 2019: *The Hindu Kush Himalaya Assessment: Mountains, Climate Change, Sustainability and People.* Springer, 627 pp., https://doi.org/10.1007/978-3-319-92288-1.

Widmann, M., and Coauthors, 2019: Current opportunities and challenges in developing hydro-climatic services in the Himalayas. Report of Pump Priming Project November 2019, 42 pp., https://nora.nerc.ac.uk/id/eprint/528847/1/N528847CR.pdf.

Wijngaard, R. R., A. F. Lutz, S. Nepal, S. Khanal, S. Pradhananga, A. B. Shrestha, and W. W. Immerzeel, 2017: Future changes in hydro-climatic extremes in the Upper Indus, Ganges, and Brahmaputra River basins. *PLOS ONE*, **12**, e0190224, https://doi.org/10.1371/journal.pone.0190224.

Wood, N., and Coauthors, 2014: An inherently mass-conserving semi-implicit semi-Lagrangian discretization of the deep-atmosphere global non-hydrostatic equations. *Quart. J. Roy. Meteor. Soc.*, **140**, 1505–1520, https://doi.org/10.1002/QJ.2235.

Wulf, H., B. Bookhagen, and D. Scherler, 2010: Seasonal precipitation gradients and their impact on fluvial sediment flux in the Northwest Himalaya. *Geomorphology*, **118**, 13–21, https://doi.org/10.1016/j.geomorph.2009.12.003.

Yang, K., T. H. Painter, J. S. Deems, and N. P. Molotch, 2025: Bias correction for near-real-time estimation of snow water equivalent using machine learning algorithms: A case study in the Tuolumne River basin, California. *Remote Sens. Environ.*, **323**, 114693, https://doi.org/10.1016/j.rse.2025.114693.

Yang, Y., and Coauthors, 2024: Assessing satellite and reanalysis-based precipitation products in cold and arid mountainous regions. *J. Hydrol. Reg. Stud.*, **51**, 101612, https://doi.org/10.1016/j.ejrh.2023.101612.

Yatagai, A., K. Kamiguchi, O. Arakawa, A. Hamada, N. Yasutomi, and A. Kitoh, 2012: APHRODITE: Constructing a long-term daily gridded precipitation dataset for Asia based on a dense network of rain gauges. *Bull. Amer. Meteor. Soc.*, **93**, 1401–1415, https://doi.org/10.1175/BAMS-D-11-00122.1.

Yin, Z.-Y., X. Zhang, X. Liu, M. Colella, and X. Chen, 2008: An assessment of the biases of satellite rainfall estimates over the Tibetan Plateau and correction methods based on topographic analysis. *J. Hydrometeor.*, **9**, 301–326, https://doi.org/10.1175/2007JHM903.1.